Impact of Lyman alpha pressure on metal-poor dwarf galaxies

Taysun Kimm[1,2]⋆, Martin Haehnelt[2], Jérémy Blaizot[3], Harley Katz[2], Léo Michel-Dansac[3], Thibault Garel[3], Joakim Rosdahl[3], Romain Teyssier[4]

[1] *Department of Astronomy, Yonsei University, 50 Yonsei-ro, Seodaemun-gu, Seoul 03722, Republic of Korea*

[2] *Kavli Institute for Cosmology and Institute of Astronomy, Madingley Road, Cambridge CB3 0HA, UK*

[3] *Univ Lyon, Univ Lyon1, Ens de Lyon, CNRS, Centre de Recherche Astrophysique de Lyon UMR5574, F-69230, Saint-Genis- Laval, France*

[4] *Institute for Computational Science, ETH Zurich, Wolfgang-Pauli-Strasse 16, CH-8093, Zurich, Switzerland*

17 January 2018

ABSTRACT

Understanding the origin of strong galactic outflows and the suppression of star formation in dwarf galaxies is a key problem in galaxy formation. Using a set of radiation-hydrodynamic simulations of an isolated dwarf galaxy embedded in a 10^{10} $M_\odot$ halo, we show that the momentum transferred from resonantly scattered Lyman-α (Lyα) photons is an important source of stellar feedback which can shape the evolution of galaxies. We find that Lyα feedback suppresses star formation by a factor of two in metal-poor galaxies by regulating the dynamics of star-forming clouds before the onset of supernova explosions (SNe). This is possible because each Lyα photon resonantly scatters and imparts $\sim$ 10–300 times greater momentum than in the single scattering limit. Consequently, the number of star clusters predicted in the simulations is reduced by a factor of $\sim$ 5, compared to the model without the early feedback. More importantly, we find that galactic outflows become weaker in the presence of strong Lyα radiation feedback, as star formation and associated SNe become less bursty. We also examine a model in which radiation field is arbitrarily enhanced by a factor of up to 10, and reach the same conclusion. The typical mass loading factors in our metal-poor dwarf system are estimated to be $\sim$ 5 − 10 near the mid plane, while it is reduced to $\sim$ 1 at larger radii. Finally, we find that the escape of ionizing radiation and hence the reionization history of the Universe is unlikely to be strongly affected by Lyα feedback.

Key words: Cosmology: dark ages, reionization, first stars – Cosmology: early Universe – galaxies: high-redshift

1 INTRODUCTION

Observations of local starbursts and Lyman break galaxies at high redshifts indicate that massive outflows are often correlated with high star formation rates (e.g. Heckman et al. 2015), suggesting that stellar feedback is probably responsible for inefficient star formation in galaxies with $L < L_*$ (Moster et al. 2013; Behroozi et al. 2013; Sawala et al. 2015; Read et al. 2017). However, how the galactic outflows are launched and how star formation is regulated remain unsolved issues.

There are several different processes which can affect the dynamics of star-forming clouds. Massive stars emit large amounts of ultraviolet (UV) photons that create over-pressurised regions which lower the density of the interstellar medium (ISM) (e.g. Matzner 2002; Krumholz et al. 2007). Absorption of ionising radiation by neutral hydrogen and dust can also impart momentum into the ISM, driving outflows of $\sim$ 30 km s^{-1} (Leitherer et al. 1999). Small-scale simulations of giant molecular clouds (GMCs) have shown

that photo-heating and radiation pressure, caused by UV photons in the absence of dust, create a porous structure inside the GMCs on a timescale of a few Myr (Dale et al. 2012; Walch et al. 2012; Gavagnin et al. 2017). 3–40 Myr after star formation, massive stars explode as Type II supernovae (SNe), each of which release a large amount of energy ($\sim 10^{51}$ erg) instantaneously. During the explosion, cosmic rays are generated through diffusive shock acceleration (e.g. Hillas 2005) that may cause a pressure gradient to build up in the circumgalactic medium (CGM) that launches winds (Breitschwerdt et al. 1991; Everett et al. 2008; Hanasz et al. 2013). In a very optically thick region, infrared (IR) photons that are re-radiated after the absorption of UV and optical photons can be scattered many times due to the high optical depths (τ) and these photons impart momentum which is significantly higher than the single-scattering value (L/c) (Murray et al. 2005; Draine 2011b; Kim et al. 2016), where L is the luminosity and c is the speed of light. Finally, radiation pressure due to resonant line radiation transfer is also known to be an important source of momentum to drive stellar winds (Castor et al. 1975; Abbott 1982).

Of these different modes of feedback, particular attention is

⋆ e-mail: tkimm@yonsei.ac.kr

paid to SNe, as it is known to generate significantly more radial momentum compared to other sources, such as stellar winds (e.g. Draine 2011a). Local simulations of a stratified medium also suggest that pressure equilibrium can be maintained by injecting the momentum from SNe (deAvillez & Breitschwerdt 2005; Joung et al. 2009b; Kim et al. 2013), although there are uncertainties regarding how to model the position of SNe (Hennebelle & Iffrig 2014; Walch et al. 2015). On the other hand, reproducing a low star formation efficiency with SNe alone appears to be a much more challenging problem in a cosmological context (Joung et al. 2009a; Aumer et al. 2013; Kimm et al. 2015; Agertz & Kravtsov 2015). This is partly because early attempts cannot capture the adiabatic phase of a SN explosion, during which radial momentum of the expanding shell is increased due to the over-pressurised medium inside the SN bubble. When the adiabatic phase is resolved, the final momentum is roughly $3 \times 10^5 \mathrm{M}_\odot \mathrm{km\,s}^{-1}$ per SN (Thornton et al. 1998; Blondin et al. 1998; Kim & Ostriker 2015; Martizzi et al. 2015), which is ~ 10 times greater than the momentum of initial SN ejecta. However, even when the correct momentum is taken into consideration, stellar masses of dwarf-sized galaxies still seem to be too massive (Hopkins et al. 2014; Kimm et al. 2015), compared to those observationally derived (e.g. Behroozi et al. 2013).

As a solution to this over-cooling problem, Murray et al. (2005) put forward an idea that IR photons exert non-thermal pressure in the ISM and launch galactic winds. Using isolated galaxy simulations, Hopkins et al. (2011) show that, when the optical depth (τ_{IR}) is estimated by the simple combination of dust column density and dust absorption cross-section, star-forming regions can easily attain a high τ_{IR} of $\sim 10 - 100$. If this is the case, the radiation pressure from IR photons may be the most important mechanism suppressing star formation and driving outflows in massive galaxies (see also Aumer et al. 2013; Hopkins et al. 2014; Agertz & Kravtsov 2015, 2016). However, estimating the effective optical depth that is relevant to actual radiation pressure does not appear to be a trivial task because dust-rich gas can be unstable against instabilities that create holes through which IR photons can escape (Krumholz & Thompson 2012; Davis et al. 2014; Rosdahl & Teyssier 2015). Furthermore, the inclusion of galactic turbulence may lead to even smaller values for optical depths (e.g. Skinner & Ostriker 2015). The first galactic-scale simulations which were fully coupled with multiply scattered IR radiation (Rosdahl et al. 2015) indeed find no evidence that star formation can be controlled by IR pressure in halos with mass $10^{10} - 10^{12} \mathrm{M}_\odot$, even though τ_{IR} may be under-estimated locally due to the finite resolution ($\sim$20 pc) adopted in the study. In an opposite regime where IR radiation pressure is able to violently destroy the gaseous disk, the effective τ_{IR} may again be significantly smaller than the value estimated from $\tau L/c$, as the photons tend to freely escape (Bieri et al. 2017).

Alternatively, SNe may be able to generate stronger outflows if multiple massive stars explode in a short period of time. The idea behind this is to minimise the radiative losses in the SN shells (Sharma et al. 2014; Keller et al. 2014), although the precise determination of the momentum boost is still being debated (Geen et al. 2016; Gentry et al. 2017; Kim et al. 2017). Nevertheless, given that the momentum from SNe depends on ambient density as $n_{\mathrm{H}}^{-2/17}$ it would not be surprising to have a more significant impact from the multiple SN events. Note that such spatially coherent SNe are already included in the existing simulations (Hopkins et al. 2014; Kimm et al. 2015). In order for super-bubble feedback to work, the extra momentum per SN has to be significantly larger than the momentum budget from a single event. The prerequisite condition for the super-bubble feedback is that gas is converted into stars very

quickly so that any type of early feedback does not intervene in the formation of massive star clusters. When a low star formation efficiency per free-fall time is employed in conjunction with strong IR radiation pressure, the ability of regulating star formation with IR photons appears to be very difficult (Agertz & Kravtsov 2015). In this regard, super-bubble feedback has an implicit dependence on radiation feedback that operates early on, and it is desirable to fully couple hydrodynamic interactions to radiation in order to self-consistently model star formation and feedback.

Recently, analysing 32 HII regions in the Small and Large Magellanic clouds, Lopez et al. (2014) conclude that pressure by warm ionized gas dominates over UV and IR radiation pressure. The result that photoionization heating by Lyman continuum (LyC) photons is vital for the understanding of the dynamics before the onset of SNe is also pointed out by several groups based on initially perturbed cloud simulations (Dale et al. 2012; Walch et al. 2012; Geen et al. 2016). The mechanism alone is unlikely to drive the strong outflows we observe in starburst galaxies, but it is potentially an important source of early feedback to clear out the surrounding medium for hot bubbles (i.e. low-density channels) so that they can propagate easily out to the intergalactic medium (Iffrig & Hennebelle 2015). Of course, since the Stromgren radius has a strong dependence on density ($r_S \propto n_{\mathrm{H}}^{-2/3}$), HII regions might be confined to a very small volume and would not play a role if young massive stars were deeply embedded in a massive GMC.

However, both the dynamics and the role of photoionization may change if strong radiation pressure that has little or a positive dependence on ambient density is present. Multiply scattered IR photons are one of those examples. Another interesting feedback source, which shares the similar characteristics as the IR pressure, is the pressure exerted by resonantly scattered Lyman α (Lyα) photons. Because $\sim 68\%$ of absorbed ionizing photons are re-emitted as Lyα photons, they create a strong emission feature in galaxies (e.g. Partridge & Peebles 1967). The main difference from IR radiation pressure is that Lyα scatters mainly by neutral hydrogen, which is virtually ubiquitous in small galaxies regardless of metallicity. Moreover, since the absorption cross-section to Lyα is extremely high, the photons are unlikely to escape even when instabilities set in. Using a simple shell model, Dijkstra & Loeb (2008) show that a multiplication factor, the measure of momentum boost, can be very high ($\gtrsim 100$) in optically thick regions, indicating that it may play a more important role than photoionization heating. Indeed, the authors demonstrate that Lyα may be able to drive winds of several tens to hundreds of $\mathrm{km\,s}^{-1}$ in the ISM. The idea is also applied to one dimensional calculations of dust-free halos to study the Lyα signature of Pop III stars (Smith et al. 2017b). Despite its potential significance, little efforts have been made to understand the impact of Lyα feedback on galaxy evolution. In this paper, we aim to investigate how Lyα feedback affects the evolution of star-forming clouds, the structure of the ISM, and whether or not it enhances galactic outflows using three dimensional radiation hydrodynamic simulations (RHDs) of isolated disc galaxies.

The outline of this paper is as follows. In Section 2, we present the physical ingredients of our simulations and describe our Lyα feedback model which is based on three dimensional Monte Carlo radiative transfer calculations. We analyse our simulations and quantify the impact of Lyα pressure on star formation, the properties of outflows and the ISM, and the formation of star clusters in Section 3. We then discuss the role of early feedback in launching strong galactic outflows and reionization of the Universe along with potential caveats and limitations of our simulations in Section 4. Finally, we summarise and conclude in Section 5.

2 SIMULATIONS

We perform isolated disk galaxy simulations using the radiation hydrodynamics code, RAMSES-RT (Teyssier 2002; Rosdahl et al. 2013; Rosdahl & Teyssier 2015). The Euler equations are evolved using a HLLC scheme (Toro et al. 1994), with the Minmod slope limiter and a courant number of 0.7. We adopt a multi-grid method to solve the Poisson equation (Guillet & Teyssier 2011). For radiative transfer, we employ a first-order moment method using the M1 closure[1] for the Eddington tensor and the Global Lax-Friedrich intercell flux function for explicitly solving the advection of radiation between cells (Rosdahl et al. 2013; Rosdahl & Teyssier 2015).

2.1 Initial conditions

Our initial condition represents a small, rotating, gas-rich, disk galaxy embedded in a $10^{10}\,\mathrm{M_\odot}$ dark matter halo. The initial conditions were originally generated with the MAKEDISK code (Springel et al. 2005), and adopted previously in Rosdahl et al. (2015, G8 runs). The only difference is the gas metallicity, which is decreased to $Z = 0.02\,Z_\odot$ to mimic galaxies at high redshifts (e.g., Maiolino et al. 2008). The galaxy has an initially warm ($T = 10^4$ K) gaseous disk, and is surrounded by hot ($T = 10^7$ K), tenuous ($n_\mathrm{H} = 10^{-7}\,\mathrm{cm^{-3}}$) halo gas. The total initial gas mass in the galaxy is $1.7 \times 10^8\,\mathrm{M_\odot}$, and the initial stellar mass is $2.0 \times 10^8\,\mathrm{M_\odot}$. The virial radius of the halo is ≈ 41 kpc, and the corresponding circular velocity is $\approx 30\ \mathrm{km\,s^{-1}}$.

The size of the simulated box is $150\,\mathrm{kpc}$, which is large enough to encapsulate the entire halo. The computational domain is filled with 128^3 root cells, which are further refined to achieve a maximum physical resolution of 4.6 pc ($\Delta x_\mathrm{min} = 150\,\mathrm{kpc}/2^{15}$). This is done by imposing two different refinement criteria. First, a cell is refined if the total baryonic plus dark matter inside each cell exceeds $8000\,\mathrm{M_\odot}$ or if the gas mass is greater than $1000\,\mathrm{M_\odot}$. Second, we enforce that the thermal Jeans length is resolved by at least 4 cells until it reaches the maximum resolution (Truelove et al. 1997).

2.2 Star formation and feedback

Star formation is modelled based on a Schmidt law (Schmidt 1959), $\rho_\mathrm{star} = \epsilon_\mathrm{ff}\rho_\mathrm{gas}/t_\mathrm{ff}$, using the Poisson sampling method (Rasera & Teyssier 2006), where ϵ_ff is a star formation efficiency per free-fall time (t_ff), and ρ_gas is the gas density. Instead of taking a fixed ϵ_ff, we adopt a thermo-turbulent scheme (Devriendt et al. 2017; Kimm et al. 2017) where ϵ_ff is determined by the combination of the local virial parameter and turbulence, as

$$\epsilon_\mathrm{ff} = \frac{\epsilon_\mathrm{ecc}}{2\phi_t}\exp\left(\frac{3}{8}\sigma_s^2\right)\left[1 + \mathrm{erf}\left(\frac{\sigma_s^2 - s_\mathrm{crit}}{\sqrt{2\sigma_s^2}}\right)\right], \quad (1)$$

where $\sigma_s^2 = \ln\left(1 + b^2\mathcal{M}^2\right)$, $s \equiv \ln\left(\rho/\rho_0\right)$, $\epsilon_\mathrm{ecc} \approx 0.5$, $\phi_t \approx 0.57$, $b \approx 0.4$, and $\mathcal{M}$ is the sonic Mach number. Here $s_\mathrm{crit} = \ln\left(0.067\,\theta^{-2}\alpha_\mathrm{vir}\mathcal{M}^2\right)$ approximates the minimum critical density

---

[1] Although the M1 scheme is known to be more diffusive than the accurate methods, such as the variable Eddington tensor (e.g. Gnedin & Abel 2001; Davis et al. 2014), the expansion of HII bubble, which is a key process that determines the number of hydrogen recombination radiation, is well described by the M1 closure, as ionizing radiation from massive stars is isotropic by nature (Bisbas et al. 2015). Thus, radiative transfer with the M1 closure for the Eddington tensor is a reasonable choice to probe the impact of Lyα pressure.

Table 1. Properties of eight photon groups used in the base model with radiation feedback excluding Lyα pressure.

Photon group	ϵ_0 [eV]	ϵ_1 [eV]	κ [cm^2/g]	Main function
EUV$_\mathrm{HeII}$	54.42	∞	10^3	HeII ionisation
EUV$_\mathrm{HeI}$	24.59	54.42	10^3	HeI ionisation
EUV$_\mathrm{HI,2}$	15.2	24.59	10^3	HI and H$_2$ ionisation
EUV$_\mathrm{HI,1}$	13.6	15.2	10^3	HI ionisation
LW	11.2	13.6	10^3	H$_2$ dissociation
FUV	5.6	11.2	10^3	Photoelectric heating
Optical	1.0	5.6	10^3	Direct RP
IR	0.1	1.0	5	Radiation pressure (RP)

above which gas can collapse, where $\alpha_\mathrm{vir} \equiv 2E_\mathrm{kin}/|E_\mathrm{grav}|$ is the virial parameter and $\theta = 0.33$ (Padoan & Nordlund 2011; Federrath & Klessen 2012). Note that we make a slight modification to the original scheme in order to allow for bursty star formation at the galactic centre. Specifically, when quantifying the local turbulence and virial parameter, we subtract the symmetric component of divergence and rotational motions. In addition, we prevent stars from forming if a gas cell in question is not a local density maxima or the gas flow is not convergent. The resulting efficiency per free-fall time ranges from ≈ 5 to 45% when a star particle is formed, with a mean ϵ_ff of $\approx 18\%$ in the case of the fiducial run with 4.6 pc resolution. The minimum mass of a star particle is $910\,\mathrm{M_\odot}$, which hosts 10 individual Type II supernova explosions for a Kroupa initial mass function (Kroupa 2001). SN explosions are modelled using the mechanical feedback scheme of Kimm & Cen (2014) with the realistic time delay (Kimm et al. 2015). For the stellar spectra, we use the BPASS model (Stanway et al. 2016) with the two different IMF slopes of -1.30 (0.1–0.5 $\mathrm{M_\odot}$) and -2.35 (0.5–100 $\mathrm{M_\odot}$).

We employ eight photon groups to account for photo-ionization heating, photo-electric heating on dust, direct radiation pressure from UV and optical photons, and non-thermal pressure from multi-scattered IR photons (Rosdahl & Teyssier 2015), as laid out in Table 1 (Kimm et al. 2017). The evolution of molecular hydrogen and primordial species (HI, HII, HeI, HeII, HeIII, e^{-1}, and H$_2$) is followed by solving the non-equilibrium photo-chemistry (see Katz et al. 2017 and Kimm et al. 2017 for details). To keep the computational costs low, we use a reduced speed of light approximation ($\tilde{c} = 10^{-3}c$), where c is the full speed of light. A uniform ultraviolet background (Haardt & Madau 2012) is included with the self-shielding approximation (Kimm et al. 2017) assuming that the simulated galaxies are at $z = 3$.

2.3 Lyman-α pressure

2.3.1 Model

Lyα photons are known to resonantly scatter in optically thick regions due to the large absorption cross-section of neutral hydrogen before they escape or get absorbed by dust (Osterbrock 1962; Adams 1972; Bonilha et al. 1979; Neufeld 1990). The number of scatterings in a dust-free medium are typically on the order of τ_0, the optical depth from the centre to the edge at the line centre (e.g. Adams 1972; Harrington 1973; Dijkstra et al. 2006). This implies that the momentum transfer from the scattering by Lyα photon can potentially be very important in the evolution of star-forming clouds.

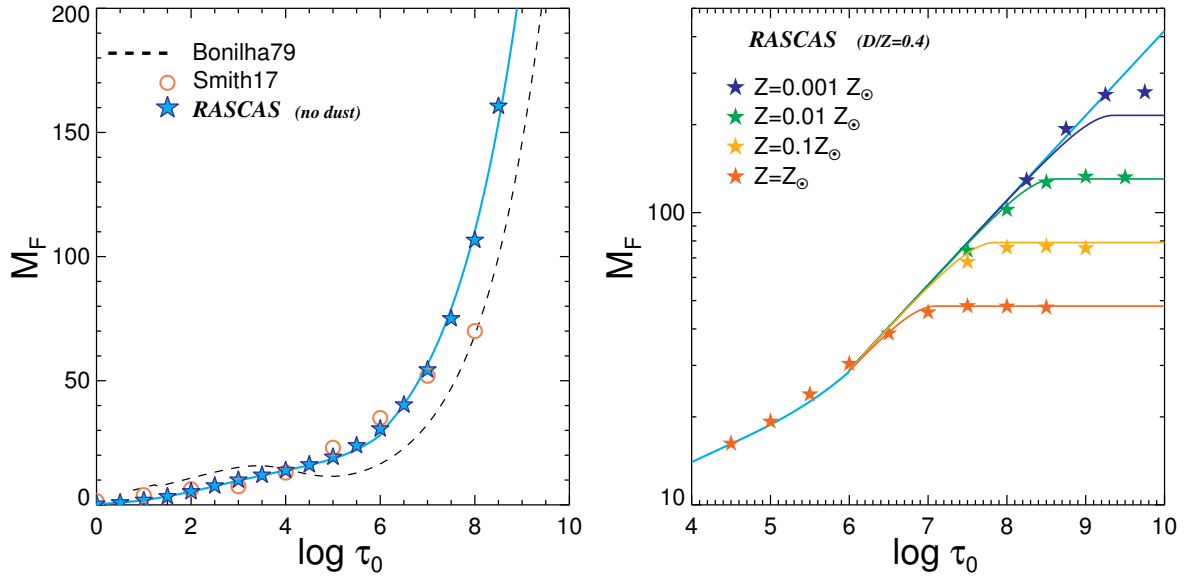The momentum transfer from resonant line transitions is usu-

Figure 1. Multiplication factor (M_F) of Lyα photons as a function of optical depth at the line centre (τ_0), computed using the Monte-Carlo Lyα radiative transfer code, RASCAS. *Left*: M_F in the dust-free medium with temperature $T = 100$ K. The dashed line indicates the results ($t_{\rm trap}/t_{\rm light} \approx M_F$) from an earlier work by Bonilha et al. (1979) with temperature $T = 10^4 K$, and the empty circles correspond to the results ($t_{\rm trap}/t_{\rm light}$) at $T = 1$ K from Smith et al. (2017b). The solid line indicates the fit to our calculations (Equations 6-7). *Right*: M_F in the presence of dust. The star symbols with different colour-codings are the results from our Monte Carlo calculations with different metallicities assuming a constant dust-to-metal ratio of 0.4. The solid lines are the fits to these results (see the text). Note that each Lyα photon can transfer $\sim$10–300 times larger momentum than the single scattering case in metal-poor environments.

ally expressed in terms of a multiplication factor (M_F), as

$$F_{Ly\alpha} = M_{\rm F} \frac{L_{Ly\alpha}}{c}, \qquad (2)$$

where $F_{Ly\alpha}$ is the force due to Lyα photons of luminosity $L_{Ly\alpha}$. Note that the optical depth to Lyα is very sensitive to the exact frequency of a photon, and, therefore, is not simply proportional to the column density of a scatterer, as is often done for IR photons. The multiplication factor can be thought of as the ratio between the time Lyα photons are trapped and the light crossing time ($t_{\rm light}$). Early works showed that M_F increases rapidly with increasing optical depth in a dust-free slab of neutral hydrogen (Adams 1972; Bonilha et al. 1979), resulting in (see Dijkstra & Loeb 2008),

$$M_{\rm F}^{\rm nodust} \approx t_{\rm trap}/t_{\rm light} \qquad (3)$$

$$\approx 15 \times \left(\tau_0/10^6\right)^{1/3} T_4^{1/6} \quad (\log \tau_0 \geq 6), \qquad (4)$$

where $t_{\rm trap}$ is the trapping time, $t_{\rm light}$ is the light crossing time of the slab, and $T_4 \equiv T/10^4$ K. The dependence of $1/3$ on the optical depth may be understood as a consequence of coherent scattering in an extremely optically thick regime (Adams 1975).

In order to probe a wider parameter space and the effects of dust, we measure M_F using a new three-dimensional Monte Carlo Lyα radiative transfer code, RASCAS (Michel-Dansac et al. *in preparation*), which is based on Verhamme et al. (2006). Monte Carlo radiative transfer (MCRT) calculations are performed with the recoil effects, the dipolar angular redistribution functions, and scattering by deuterium with the abundance ($D/H = 3 \times 10^{-5}$). We adopt a dust albedo of $\mathcal{A}_b = 0.46$ and the extinction cross-section per hydrogen nucleus of $\sigma_d = 3 \times 10^{-21}$ cm^2/H at solar metallicity ($Z_\odot = 0.02$). The latter is slightly higher than Weingartner & Draine (2001) and is thus a conservative estimate in terms of Lyα pressure.

We first place a Lyα emitting stellar source at the centre of a uniform medium with temperature $T = 100$ K and compute the

momentum transfer at each scattering event from $N_{\rm Lya} = 10^4$ photons, as

$$\Delta \vec{p} = \frac{h_p}{c} \left(\nu_{\rm in}\hat{n}_{\rm in} - \nu_{\rm out}\hat{n}_{out}\right). \qquad (5)$$

Here $\nu_{\rm in}$ and $\nu_{\rm out}$ are the frequency before and after a scattering, $\hat{n}$ denotes a direction vector, and h_p is the Planck constant. We then measure the *net radial momentum* centred on the stellar source, and divide it by the momentum due to a single Lyα scattering event to obtain M_F. The resulting M_F is shown as a function of optical depth ($\tau_0 = \sigma_0 N_{\rm HI}$) at the line centre ($\nu_0 = 2.466 \times 10^{15}$ Hz) in Figure 1, where $\sigma_0 = 5.88 \times 10^{-14}$ cm$^2 T_4^{-1/2}$ is the absorption cross-section for Lyα. The dust-free M_F may be fit from the Monte Carlo results (starred points in Figure 1) as

$$M_{\rm F}^{\rm nodust} \approx 29 \left(\frac{\tau_0}{10^6}\right)^{0.29} \quad \left(\tau_0 \geq 10^6\right), \qquad (6)$$

$$\log M_{\rm F}^{\rm nodust} \approx -0.433 + 0.874 \log \tau_0 - 0.173 \left(\log \tau_0\right)^2$$
$$+ 0.0133 \left(\log \tau_0\right)^3 \qquad \left(\tau_0 < 10^6\right) \qquad (7)$$

It can be seen that our measurements are largely consistent with the low temperature results from Smith et al. (2017b). M_F tends to be higher than those from the experiments with a higher temperature ($T = 10^4$ K, Bonilha et al. 1979), but this is expected, as Lyα photons are trapped by the wing opacity, which is proportional to the Voigt parameter $a_V = 4.7 \times 10^{-4} T_4^{-1/2}$ (Adams 1972, 1975), in the optically thick regime.

If dust is present and destroys Lyα photons, M_F cannot simply increase as $\propto \tau_0^{0.29}$ in the optically thick regime. Instead, one can expect that M_F saturates to a maximum value for a given optical depth, as the majority of Lyα photons are absorbed by dust. The right panel of Figure 1 demonstrates that in metal-rich, dusty environments, M_F cannot be more than ≈ 50, whereas it can eas-

ily be as high as ≈ 300 in metal-poor ($Z = 0.01\,Z_\odot$), less dusty ($D/M = 0.04$) regions.

In order to properly model the momentum transfer from the scattering of Lyα photons, one should of course couple the Lyα MCRT to the RHD equations (see Smith et al. 2017b, for a one dimensional example). However, this is not computationally feasible for three dimensional problems unless a specially designed algorithm, such as the discrete diffusion MC methodology (Smith et al. 2017a), is used. Instead, we introduce a sub-grid model that can be used in our RHD simulations as follows. Since lower escape fractions of Lyα photons indicate that dust destroys Lyα photons more efficiently and limits the impact from Lyα pressure, we use the functional form of the escape fractions to find a fit that reasonably matches M_F in Fig. 1 (right panel). In an optically thick slab, the escape fractions may be approximated as (Neufeld 1990; Hansen & Oh 2006; Verhamme et al. 2006),

$$f_{\rm esc}^{\rm Ly\alpha} = 1/\cosh\left\{\frac{\sqrt{3}}{\pi^{5/12}\xi}[(a_V\tau_0)^{1/3}\tau_{\rm da}]^{1/2}\right\}, \qquad (8)$$

where $\tau_{\rm da} = N_{\rm HI}f_{\rm d/m}Z'\,\sigma_d(1-\mathcal{A}_b)$, $\xi = 0.525$ is a fitting parameter, $Z' \equiv Z/Z_\odot$, and $f_{\rm d/m}$ is the dust-to-metal mass ratio, normalised to the value at solar metallicity. Note that Eq. 8 describes the fraction of Lyα photons that is eventually destroyed, hence a simple combination of $M_F^{\rm nodust}f_{\rm esc}^{\rm Ly\alpha}$ cannot be used as a proxy for M_F in dusty environments (c.f., Bithell 1990). Instead, we note that the local maximum of $\left(M_F^{\rm nodust} \times f_{\rm esc}^{\rm Ly\alpha}\right)$ gives a *minimum* estimate of the asymptotic value of $M_{\rm F,dust}$. We find this numerically by defining

$$y \equiv \frac{\sqrt{3}}{\pi^{5/12}\xi}\left[(a_V\,\tau_0)^{1/3}\,\tau_{\rm da}\right]^{1/2}. \qquad (9)$$

For the optical depth with a functional form of $M_F \propto \tau_0^{0.29}$, the local maximum occurs at $y_{\rm peak} = 0.71134$. Note that M_F is likely to be higher than this, because destroyed photons can also contribute to the total momentum before they get absorbed. To account for this, we modify the escape fractions by adjusting $\xi \to \xi_{\rm fit} = 1.78$ so that it can reproduce the momentum transfer calculations from MCRT reasonably well (Figure 1, right). The resulting optical depth at which $M_F^{\rm nodust}f_{\rm esc}(\xi \to \xi_{\rm fit})$ reaches a peak may be written as

$$\tau_0^{\rm peak} = \left(\frac{\pi^{5/12}\xi_{\rm new}}{\sqrt{3}}\,y_{\rm peak}\right)^{3/2}\left[\frac{1}{a_V^{1/3}(1-\mathcal{A}_b)f_{\rm d/m}Z'}\left(\frac{\sigma_0}{\sigma_d}\right)\right]^{3/4}$$
$$= 4.06 \times 10^6\, T_4^{-1/4}\, \left(f_{\rm d/m}\,Z'\right)^{-3/4}\left(\frac{\sigma_{\rm d,-21}}{3}\right)^{-3/4} \qquad (10)$$

Here $\sigma_{\rm d,-21} \equiv \sigma_d/10^{-21}\,{\rm cm}^2/{\rm H}$.

It is worth mentioning that the multiplication factor relies on the temperature of the medium (Adams 1975; Smith et al. 2017b). We perform the MCRT with a fixed temperature $T = 100\,{\rm K}$, because this is the typical temperature of star-forming clouds under the influence of photoelectric heating on dust. If Lyα photons mostly reside in the warm ISM ($T \sim 10^4\,{\rm K}$), our model is likely to over-estimate the non-thermal pressure, although the dependence on temperature is not very strong ($\propto T^{-1/6}$) (Adams 1975). However, it should be noted that warm gas exists mostly when ionizing radiation is locally very intense or SN explosions are energetic enough to drive winds at which point the Lyα force is no longer the only dominant mechanism. Therefore, we believe it is more appropriate to use the multiplication factor at low temperatures to investigate the impact of Lyα feedback.

2.3.2 Subgrid implementation

In practice, we include the momentum transfer from multi-scattered Lyα photons as follows.

1. We first estimate the local Lyα emissivity in every cells by computing the radiative recombination rates

$$\epsilon_{\rm rec,Ly\alpha} = P_B(T)\,\alpha_B(T)\,n_e\,n_{\rm HII}\,e_{\rm Ly\alpha}, \qquad (11)$$

where $e_{\rm Ly\alpha}$ is the energy of individual Lyα photon (10.16 eV), n_e and $n_{\rm HII}$ are the number density of electron and ionized hydrogen, $P_B(T) = 0.686 - 0.106\log T_4 - 0.009\,T_4^{-0.44}$ is the probability for absorbed Lyman continuum photons to emit a Lyα photon (Cantalupo et al. 2008), and α_B is the case-B recombination coefficient (Hui & Gnedin 1997),

$$\alpha_B = 2.753 \times 10^{-14}\,{\rm cm}^3\,{\rm s}^{-1}\frac{\lambda^{1.5}}{\left[1 + (\lambda/2.74)^{0.407}\right]^{2.242}}, \qquad (12)$$

where $\lambda = 315614\,{\rm K}/T$. Ly$\alpha$ photons are also produced through collisional excitation process (e.g., Callaway et al. 1987), but we find that this is a very minor contribution (see also Rosdahl & Blaizot 2012; Dijkstra 2014). From Equation 11, we compute the total number of Lyα photons produced in each cell per simulation time step, and take the maximum between this and the actual number of ionizing photons absorbed times $P_B(T)$, as

$$N_{\rm Ly\alpha} = \max\left[\epsilon_{\rm rec,Ly\alpha}\Delta V\Delta t/e_{\rm Ly\alpha}, N_{\rm LyC}^{\rm abs}P_B(T)\right], \qquad (13)$$

where ΔV is the volume of the cell, Δt is the fine time step, and $N_{\rm LyC}^{\rm abs}$ is the total number of LyC photons absorbed during Δt. The latter term is necessary, because the ionized fraction of hydrogen is often under-estimated in dense cells where the Stromgren sphere is not fully resolved.

2. Then, we estimate the multiplication factor (M_F). To do so, we compute the local column density using the Sobolev-type approximation (Gnedin et al. 2009), as $N_{\rm HII} \approx n_{\rm HI}l_{\rm Sob}$, where $l_{\rm Sob} = \max(\rho/|\nabla\rho|, \Delta x)$. Note that this should give a reasonable approximation as long as the optical depth (τ_0) is large enough to give a value close to the maximum multiplication factor. Once we compute $\tau_0^{\rm peak}$ from Equation 10 and the corresponding column density ($N_{\rm HI}^{\rm peak} = \tau_0^{\rm peak}/\sigma_0$), the multiplication factor can be obtained from Equations 6–8, as

$$M_F = M_F^{\rm nodust}(\tau_0') \times f_{\rm esc}^{\rm Ly\alpha}(N_{\rm HI}', \xi_{\rm fit}), \qquad (14)$$

where

$$\tau_0' = \min(\tau_0, \tau_0^{\rm peak}) \quad ; \quad N_{\rm HI'} = \min(N_{\rm HI}, N_{\rm HI}^{\rm peak}). \qquad (15)$$

3. We then impart a momentum of

$$\Delta\vec{p} = M_F\frac{N_{\rm Lya}\,e_{\rm Lya}}{c}\hat{n} \qquad (16)$$

using the flux-weighted average directions ($\hat{n}$) of ionizing photon groups[2]. This method, however, cannot be used for the cell in which young star particles reside, because photons are emitted isotropically. Therefore, we take care of these cells with young stars ($t \leq 50\,{\rm Myr}$) separately, and inject the radial momentum

---

[2] Since the momentum transfer from Lyα photons in a homogeneous medium is expected to be spherically symmetric with respect to the stellar source, we adopt the directions of LyC photons, which carry the information about the location of dominant stellar sources around the cell of interest, as a simple approximation.
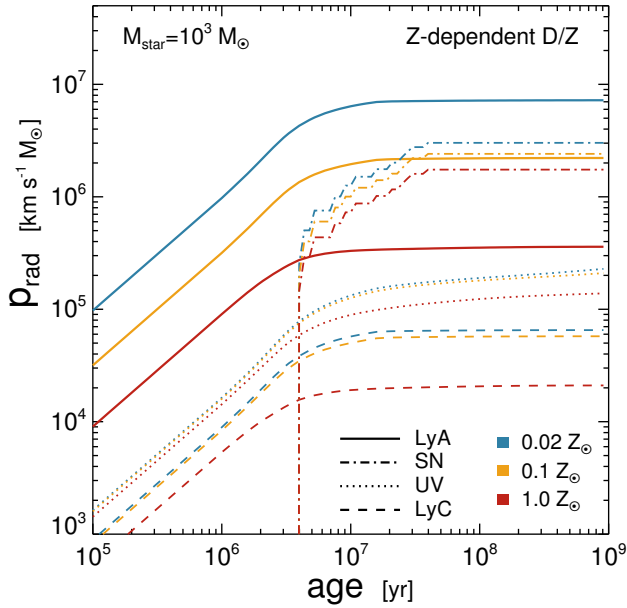
Figure 2. Integrated radial momentum from an SSP of $M_{\rm star} = 10^3\,{\rm M_\odot}$ based on the BPASS spectra. The momentum budget from LyC ($\lambda < 912\mathring{A}$, dashed), UV ($\lambda < 3000\mathring{A}$, dotted), SN (dot-dashed), and Lyα (solid) is shown with different line styles, as indicated in the legend. Different colour-codings denote different metallicities. To estimate the momentum from SNe, we randomly sample the time delay for 11 SNe, appropriate for the Kroupa IMF, assuming that they all explode in dense environments ($n_{\rm H} = 100\,{\rm cm^{-3}}$). Note that the momentum would be augmented by a factor of ~ 3 if SN explodes at much lower densities ($n_{\rm H} = 0.01\,{\rm cm^{-3}}$). The momentum from Ly$\alpha$ is estimated assuming the metallicity-dependent dust-to-gas ratios (see text). One can see that momentum transfer from Lyα pressure is significant particularly at low metallicities.

isotropically to 18 neighbouring cells, as is done for the transfer of momentum from SN explosions. Note that we limit the change in velocity to $|\Delta v| \leq 100\,{\rm km\,s^{-1}}$ per fine time step, because occasionally around low-density ionization fronts, the velocity change is over-estimated due to our simple assumption of a static medium during acceleration[3]. When momentum is cancelled out, we transfer kinetic energy to thermal energy. We also note that this approach will neglect any Lyα photons escaping from their birth place (i.e. birth cell), which can potentially enhance the non-thermal pressure. We discuss this issue in Section 4.

In Figure 2, we compare the relative importance of the momentum transfer from Lyα pressure with those from other processes in a metal-poor environment ($Z_{\rm gas} = 0.02\,{\rm Z_\odot}$). We adopt the spectral energy distributions from the BPASS v2 model with the maximum stellar mass cut-off of $100\,{\rm M_\odot}$ (Stanway et al. 2016), and assume that $\approx 68\%$ of LyC photons give rise to Lyα photons. Note that we use a higher metallicity grid ($Z = 0.001$) for stars, as

---

[3] In realistic situations, the multiplication factor would drop by an order of magnitude as the velocity of expanding shells increases to $100\,{\rm km\,s^{-1}}$ (Dijkstra & Loeb 2008). On the other hand, Lyα feedback is significant inside star-forming clouds where the escape velocity is on the order of $10\,{\rm km\,s^{-1}}$. Indeed, we find that the inclusion of Lyα feedback alone does not generate hot winds ($T \gtrsim 10^5\,{\rm K}$). We also confirm that limiting the velocity change to $|\Delta v| \leq 30\,{\rm km\,s^{-1}}$ does not make a significant difference.

this is the lowest metallicity grid available in the BPASS v2 model. We also consider the metallicity-dependent dust-to-metal mass ratio ($f_{\rm d/m}$), normalised to the value at solar metallicity, in our simulations, based on the $X_{\rm CO,z}$ case fitted with the broken power law from Rémy-Ruyer et al. (2014), as

$$\log f_{\rm d/m} = 0 \qquad\qquad (x > 8.10),$$
$$= 1.25 - 2.10 \times (x_\odot - x) \qquad (x \leq 8.10), \qquad (17)$$

where $x \equiv 12 + \log{(O/H)}$ and $x_\odot = 8.69$. This means that the dust-to-metal ratio we adopt at $Z = 0.02\,{\rm Z_\odot}$ is ≈ 200 times smaller than the values usually found in the Milky Way (Draine et al. 2007; Galametz et al. 2011). For comparison, we also include the momentum input from LyC ($\lambda < 912\mathring{A}$) and UV ($\lambda < 3000\mathring{A}$) photons. For the contribution from SNe, we randomly sample the delay time distributions using the method described in Kimm et al. (2015), which is based on the SN II rates from STARBURST99 (Leitherer et al. 1999).

Figure 2 illustrates that resonantly scattered Lyα in metal-poor ($Z \lesssim 0.1\,{\rm Z_\odot}$), dense environments ($n_{\rm H} \geq 100\,{\rm cm^{-3}}$) can transfer as much radial momentum ($p_{\rm rad}$) as SNe even before massive stars ($> 8\,{\rm M_\odot}$) evolve off the main sequence. On the other hand, because Lyα photons are efficiently destroyed by dust, their pressure is likely to be sub-dominant compared to SNe in Milky Way-like galaxies or metal-rich, massive ($M_\star \gtrsim 10^{10}\,{\rm M_\odot}$) systems at high redshift (e.g. Maiolino et al. 2008). Nevertheless, it is worth noting that Lyα pressure can still drive substantially faster winds (by an order of magnitude), compared to direct radiation pressure from LyC or UV photons. One can also see that $p_{\rm rad}$ from Lyα has a stronger dependency on metallicity compared to that from UV photons, which is mainly due to the Z-dependent $f_{\rm d/m}$ we assume.

It is also useful to compare the effect of Lyα pressure with that of photo-ionization. The maximum extent to which Lyα pressure can overcome the external pressure set by the ISM can be calculated as

$$n_{\rm H} k_B T = \frac{M_F L_\alpha}{4\pi r_\alpha^2 c} \qquad (18)$$

and thus

$$r_\alpha = \sqrt{\frac{M_{\rm F} L_\alpha}{4\pi c\, n_{\rm H}\, k_{\rm B}\, T}} \qquad (19)$$
$$\approx 37\,{\rm pc} \left(\frac{M_{\rm F}}{100}\right)^{1/2} \left(\frac{m_{\rm star}}{10^3\,{\rm M_\odot}}\right)^{1/2} \left(\frac{P/k_{\rm B}}{10^5\,{\rm cm^{-3}\,K}}\right)^{-1/2}.$$

This turns out to be larger than the maximum extent to which photo-ionization heating can counter-balance the external pressure in most environments ($10^4 \leq P/k_B \leq 10^6\,{\rm cm^{-3}\,K}$) (Rosdahl & Teyssier 2015),

$$r_{\rm PH} \approx 26\,{\rm pc} \left(\frac{m_{\rm star}}{10^3\,{\rm M_\odot}}\right)^{1/3} \left(\frac{P/k_{\rm B}}{10^5\,{\rm cm^{-3}\,K}}\right)^{-3/2} \left(\frac{T_{\rm ion}}{10^4\,{\rm K}}\right)^{2/3}. \qquad (20)$$

In particular, while $r_{\rm PH}$ decreases to sub parsec values if a star particle is deeply embedded in a star formation cloud with $P/K \sim 10^6\,{\rm cm^{-3}\,K}$, $r_\alpha \sim 20\,{\rm pc}$ still remains above our resolution. This means that including Lyα is also advantageous from a computational viewpoint, as reasonably high resolution cells should be able to capture this process. In addition, it would help to better resolve the Stromgren sphere near young stars by lowering the density into which LyC photons propagate.

Table 2. Summary of idealised disk simulations embedded in a 10^{10} M$_\odot$ dark matter halo. From left to right, each column indicates the name of the model, whether or not the simulations are performed with on-the-fly radiative transfer, the minimum size of the computational cells, the inclusion of mechanical SN feedback, Lyα pressure, photoionization heating (PH), direct radiation pressure by UV (DP) and radiation pressure by multi-scattered IR photons (IR), photoelectric heating on dust (PEH), the metallicity of gas, and some remarks.

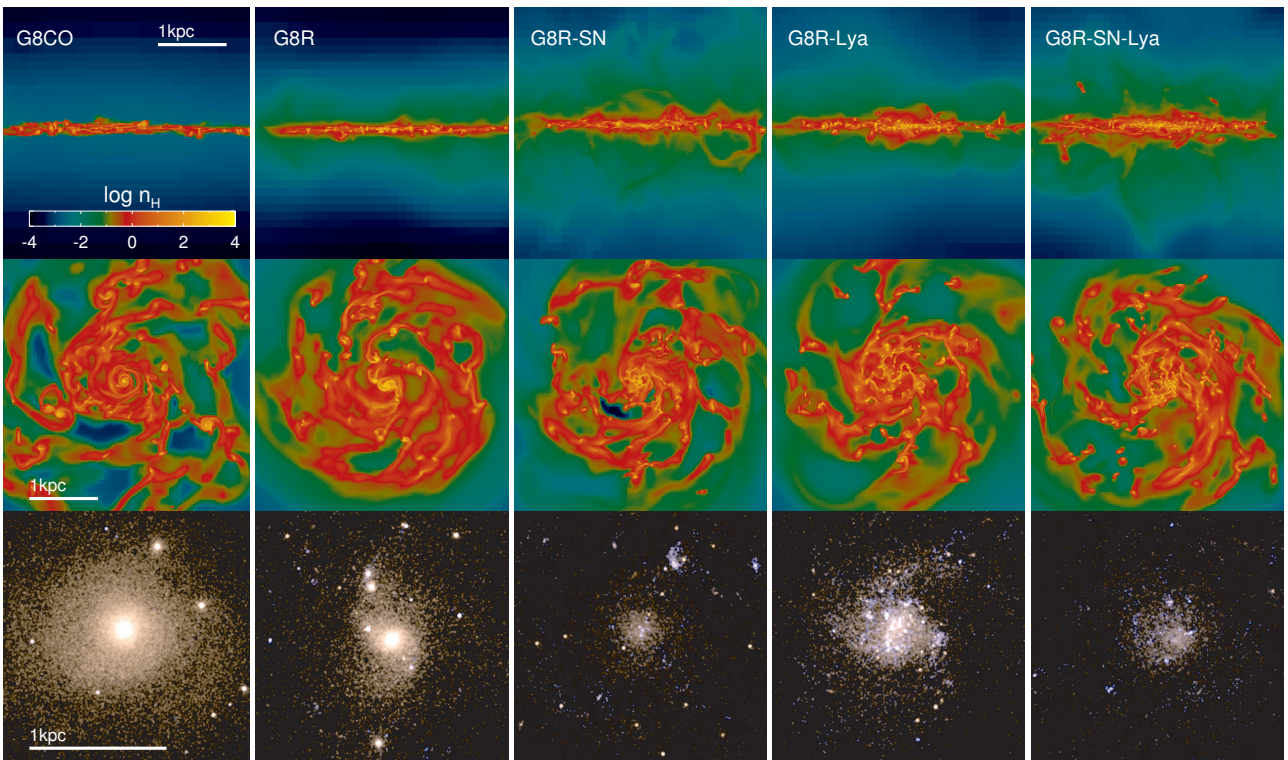| Model	RHD	$\Delta x_{\min}$	$m_{\mathrm{star}}^{\min}$	SN II	Lya	PH	DP	IR	PEH	Metallicity	Remarks
G8CO	–	4.6 pc	910 M$_\odot$	–	–	–	–	–	–	0.02 Z$_\odot$	
G8SN	–	4.6 pc	910 M$_\odot$	✓	–	–	–	–	–	0.02 Z$_\odot$	
G8R	✓	4.6 pc	910 M$_\odot$	–	–	✓	✓	✓	✓	0.02 Z$_\odot$	
G8R-SN	✓	4.6 pc	910 M$_\odot$	✓	–	✓	✓	✓	✓	0.02 Z$_\odot$	
G8R-Lya	✓	4.6 pc	910 M$_\odot$	–	✓	✓	✓	✓	✓	0.02 Z$_\odot$	
G8R-SN-Lya	✓	4.6 pc	910 M$_\odot$	✓	✓	✓	✓	✓	✓	0.02 Z$_\odot$	Fiducial
G8R-SN-Lya-f3	✓	4.6 pc	910 M$_\odot$	✓	✓	✓	✓	✓	✓	0.02 Z$_\odot$	$L_{\mathrm{star}} \times 3$
G8R-SN-Lya-f10	✓	4.6 pc	910 M$_\odot$	✓	✓	✓	✓	✓	✓	0.02 Z$_\odot$	$L_{\mathrm{star}} \times 10$
G8R-SN-Lya-s10	✓	4.6 pc	910 M$_\odot$	✓	✓	✓	✓	✓	✓	0.02 Z$_\odot$	$\epsilon_{\mathrm{ff}} \times 10$

Figure 3. Projected gas distributions of isolated disk simulations with different input physics at $t = 500\,\mathrm{Myr}$. The top and middle panels show the edge-on and face-on view of the simulated galaxy, respectively. The bottom panels show the composite stellar image using GALEX NUV, SDSS g, and i bands. Note that a smaller area is displayed for the stellar maps. Bluer colours correspond to younger stars. The white scale bar denotes $1\,\mathrm{kpc}$.

3 RESULTS

In this section, we examine the impact of radiation pressure from multi-scattered Lyα photons on galactic properties. For this purpose, we run seven RHD simulations of an isolated disk embedded in a 10^{10} M$_\odot$ dark matter halo with different input physics, as outlined in Table 2. Also performed without the on-the-fly radiative transfer are G8CO and G8SN where we turn off local radiation and Lyα pressure. Thus, the uniform background UV radiation is the only feedback source in the former case, while SNe are the main energy source that governs the dynamics of the ISM in the latter. We use these models to isolate the effects of radiation feedback (photoionization heating, radiation pressure by UV and IR photons, and photoelectric heating on dust) from other processes.

3.1 Suppression of star formation

We begin by investigating the suppression of star formation (SF) by different feedback processes. Figure 3 presents the projected gas distributions, and the composite images of SDSS u,g,i bands for stellar components. We generate these mock images by attenuating the stellar spectra using the method described in Devriendt et al. (2010), which is based on the Milky way extinction curve (Cardelli et al. 1989) and the empirical calibration by Guiderdoni & Rocca-Volmerange (1987).

The run without any feedback source (G8CO) produces a massive stellar core at the galactic centre, which is usually found in simulated galaxies suffering from artificial radiative losses (e.g. Katz 1992; Agertz et al. 2013; Hopkins et al. 2014; Kimm et al. 2015).
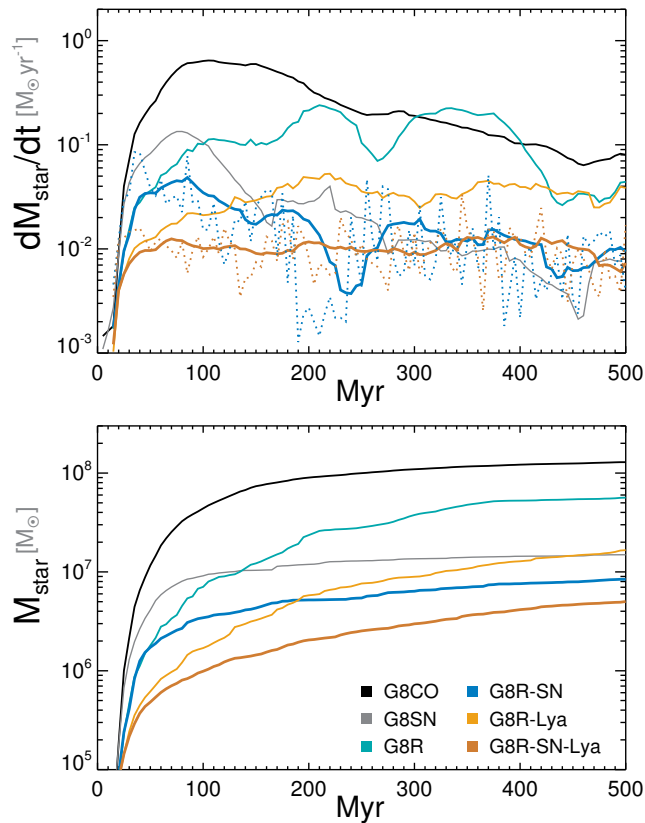
Figure 4. *Top panel*: Star formation histories of the simulated galaxy with different feedback processes, as indicated in the legend. We average the star formation rates over 50 Myr to make the comparison easier (solid lines). Also included as dotted lines are the star formation rates averaged over shorter timescale (5 Myr) for G8R-SN and G8R-SN-Lya models. Note that star formation based on the thermo-turbulent model is generally bursty. *Bottom panel*: The integrated stellar mass formed as a function of time. The inclusion of Lyα pressure regulates the star formation in the early phase, and reduces the total stellar mass by a factor of two compared to the run without it.

Even the model with the three well-known radiation feedback processes (photo-ionization heating + radiation pressure by UV and IR photons, G8R) cannot prevent the formation of the massive stellar core. The insignificance of radiation pressure by UV photons is not surprising, given that the momentum budget is not substantial (e.g. Leitherer et al. 1999; Kimm et al. 2017). IR pressure is not strong either, because the optical depth to IR photons is small in these types of metal-poor systems (Hopkins et al. 2012; Rosdahl et al. 2015). The impact of photoelectric heating on dust is also expected to be minimal because the amount of dust is negligible, although the star-forming regions are heated to $\sim 100\,\mathrm{K}$ from $\sim 10\,\mathrm{K}$ (see also Hu et al. 2017, c.f. Forbes et al. 2016). In contrast, photoion-ization heating exerts extra pressure on the ISM (Krumholz et al. 2007; Dale et al. 2012; Gavagnin et al. 2017), delaying runaway gas collapse (Rosdahl et al. 2015). This is evident by comparing the two runs, G8SN and G8R-SN, where purely hydrodynamic simulations form a lot more stars in the early phase. Figure 4 shows that the stellar mass is reduced by a factor of ~ 2 at 500 Myr when radiation feedback is included.

More interestingly, we find that Lyα pressure can suppress SF further by a factor of ~ 5 compared to the run with three
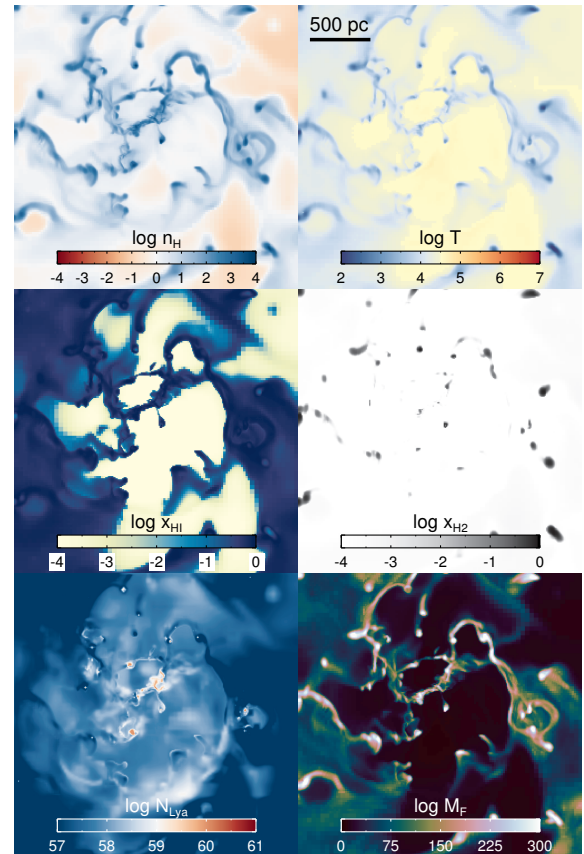

Figure 5. An example of the projected distribution of Lyα multiplication factor in the central region of the G8R-Lya run at $t = 500\,\mathrm{Myr}$. The panels show the density, temperature, neutral hydrogen fraction (x_{HI}), molecular hydrogen fraction ($x_{\mathrm{H_2}}$), number of Lyα photons produced in each cell (N_{Lya}), and the multiplication factor (M_F).

well-known radiation processes (G8R vs G8R-Lya, Figure 4). The dense stellar core found in the G8R run no longer exists (Figure 3), as the massive gas cloud at the galactic centre is efficiently dispersed. This is more evident in Figure 5 where we plot the central region of the G8R-Lya run. The size of molecular clouds are significantly smaller ($l \lesssim 100\,\mathrm{pc}$) than the massive cloud found in G8CO or G8R ($\sim 200 - 500\,\mathrm{pc}$) (Figure 3). It is worth noting that Lyα pressure operates essentially on star-forming cloud scales, as the number of LyC photons that generate Lyα photons falls precipitously as $\propto d^{-2}$, where d is the distance from the source (Figure 5). Moreover, since scattering of Lyα requires neutral hydrogen, this mechanism is effective only in the cold ISM. The multiplication factor is close to zero in the ionized, warm ISM, whereas it is maximised (~ 300) in the cold dense phase. Note that in this figure we compute M_F by counting molecular hydrogen as part of the neutral hydrogen, because it is readily destroyed by Lyman-Werner radiation near hot stars.

As discussed in Figure 2, Lyα pressure plays an important role even before the onset of SN explosions. The G8R-Lya run shows a significantly less SF than the G8R-SN run during the initial collapsing phase (Figure 4). The overall SF histories also appear more smooth in the presence of Lyα pressure, as the feedback comes into play during the early evolution of individual clouds and prevents too many stars from forming. This process is quite different from the way SNe work in the sense that a big burst of SF
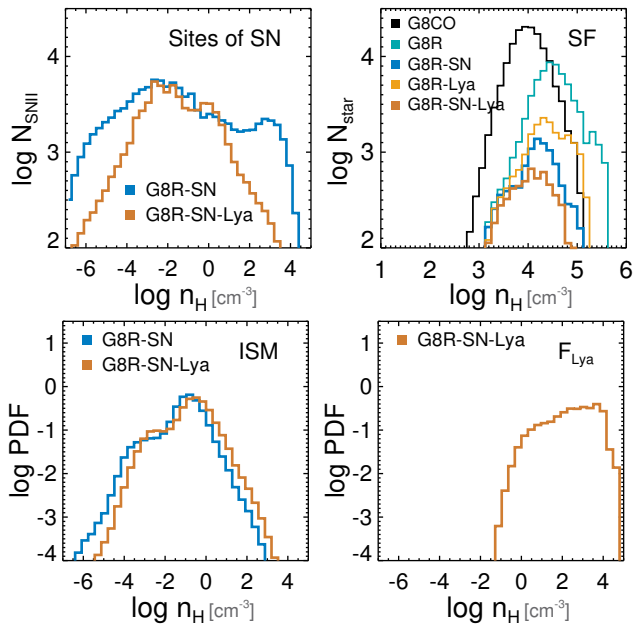
Figure 6. Distributions of densities at which SN explodes (top left) and star particles are formed (top right). The dense gas ($n_H \gtrsim 100 \, cm^{-3}$) is efficiently dispersed before the onset of SNe in the presence of Lyα pressure in the metal-poor system. The fraction of star particles formed at very high densities ($n_H \gtrsim 10^4 \, cm^{-3}$) is also reduced. The bottom left panel shows the volume-weighted density distributions of the ISM around the central mid-plane ($\sqrt{x^2 + y^2} < r_{\text{half,m}}$ and $|z| < H$), where $r_{\text{half,m}}$ is the half-mass radius and H is the scaleheight (see text). The bottom right panel indicates the volume-weighted densities at which Lyα force ($\propto N_{\text{Lya}} M_F$) is significant.

leads to strong outflows, which in turn suppresses SF, leaving the histories bursty.

Although the radial momentum imparted from Lyα can be more significant than that from SNe in dense regions (Figure 2), we find that the regulation of SF is slightly more efficient in the run with SNe (G8R-SN) than in the run with Lyα (G8R-Lya). This is because a large fraction of SNe explode in low density environments ($n_H \sim 10^{-2} \, cm^{-3}$) due to spatially correlated explosions from a realistic time delay in our dwarf-sized galaxy (Figure 6, Kimm et al. 2015). Since the momentum input from SNe is dependent on the ambient density ($p_{SN} \propto n_H^{-2/17}$), it is enhanced by a factor of three, compared to the explosions occurring inside a GMC which has a mean density, $n_H \sim 100 \, cm^{-3}$. Moreover, while SNe are an impulsive process, Lyα pressure imparts momentum continuously over several Myrs. Thus, the radial momentum from Lyα may be counter-balanced by ram pressure and self-gravity of clouds that act on a free-fall timescale of a few Myr.

The stellar mass of the simulated galaxy is further reduced by 40%, compared to the G8R-SN case, when both Lyα and SN feedback are included (G8R-SN-Lya). Most of the suppression occurs during the early phase ($t \lesssim 200 \, Myr$) outside the half-mass radius ($r_{\text{eff,m}} = 0.44 \, kpc$) where star clusters form sporadically. The total mass formed outside $r = 0.5 \, kpc$ over 500 Myr period is $M_{\text{form,out}} = 2.1 \times 10^6 \, M_\odot$ (G8R-SN-Lya), whereas it is roughly twice greater ($M_{\text{form,out}} = 5.0 \times 10^6 \, M_\odot$) in G8R-SN. In contrast, a similar amount of stars are formed in the central region ($r \leq 0.5 \, kpc$) ($M_{\text{form,in}} = 3.4 \times 10^6 \, M_\odot$ vs. $M_{\text{form,in}} = 2.9 \times 10^6 \, M_\odot$). This happens because there is a larger amount of gas in the inner region in G8R-SN-Lya ($M_{\text{gas,in}}^{\text{noLya}} \sim 2 \times 10^7 \, M_\odot$)

than in G8R-SN ($M_{\text{gas,in}}^{\text{Lya}} \sim 10^7 \, M_\odot$). The gas is less efficiently blown away from the galaxy due to a less bursty star formation history and falls back to the central region (see the next section). As a result, the difference in stellar mass becomes less prominent at late times.[4]

Hennebelle & Iffrig (2014); Walch et al. (2015) demonstrate that the choice of SN driving, i.e. where the SN explosions should be placed, leads to vastly different star formation histories. This is because SN bubbles cannot propagate efficiently if they explode in dense pockets of gas (Iffrig & Hennebelle 2015). Thus, understanding the local conditions for SNe is an important step towards a complete picture of the evolution of the ISM. Figure 6 (top left panel) shows that the number of SNe exploding in dense environments is very sensitive to the radiation feedback. More diffuse gas tend to surround young massive stars in the G8R-SN-Lya run, whereas still some number of SNe explode in dense regions in G8R-SN ($n_H \geq 100 \, cm^{-3}$). The inclusion of Lyα photons also reduces the number of SNe exploding in low-density regions ($n_H \lesssim 10^{-3} \, cm^{-3}$), as SNe become less correlated. Given that the typical density at which SNe explode better matches that of volume-filling gas (bottom left) than that of the star-forming regions (top right), our results suggest that the random SN driving model, which leads to the most significant outflows (Walch et al. 2015), may be the most relevant situation under strong radiation pressure. We also find that the number of stars born in a very dense medium ($n_H \gtrsim 10^4 \, cm^{-3}$) is decreased (top right) in the G8R-SN-Lya run, as momentum change due to Lyα pressure ($\propto N_{\text{Lya}} M_F$) is strong at high densities (bottom right). We can confirm that the local virial parameter in the star-forming regions is increased as well, indicating that the star-forming gas becomes less gravitationally bound.

3.2 Galactic outflows

Galactic outflow rates are a useful measure of the strength of stellar feedback. The results from cosmological simulations suggest that high-z dwarf galaxies should host strong outflows with an $\dot{m}_{\text{out}}$ greater in magnitude than the star formation rates in order to reproduce the observationally derived stellar mass, rotation curves, and gas metallicities in dwarf-sized galaxies (Finlator & Davé 2008; Kimm et al. 2015; Muratov et al. 2015). Local observations of small starburst systems (Heckman et al. 2015; Chisholm et al. 2017) also seem to suggest a mass-loading factor greater than unity ($\eta_{\text{out}} \gtrsim 1$), which is defined as the ratio of mass outflow and star formation rates.

In Figure 7, we show the mass outflow rates of our simulated galaxies, which are measured by computing the mass flux at $|z| = 2 \, kpc$ and $|z| = 8.2 \, kpc \, (= 0.2 \, R_{\text{vir}})$. Since the initial gas distributions are not under hydrostatic equilibrium, some gas leaves the mid plane, leading to an initial outflow. This is the major cause of the outflows before $t \lesssim 150 \, Myr$ in the runs with very weak feedback (G8CO and G8R), although cloud-cloud interactions occasionally give rise to outflowing events (e.g., $t \approx 400$-500 Myr).

We find that the outflows are strongest in the G8R-SN and G8SN runs. These models show a similar mass flux at the two different heights ($|z| = 2$ and 8.2 kpc), which indicates that SNe

---

[4] This implies that the suppression due to Lyα pressure might not be as significant as found in this study if gas accretion onto metal-poor galaxies occurs smoothly at high redshifts (c.f. Kimm & Cen 2014; Hopkins et al. 2014; Wise et al. 2014).
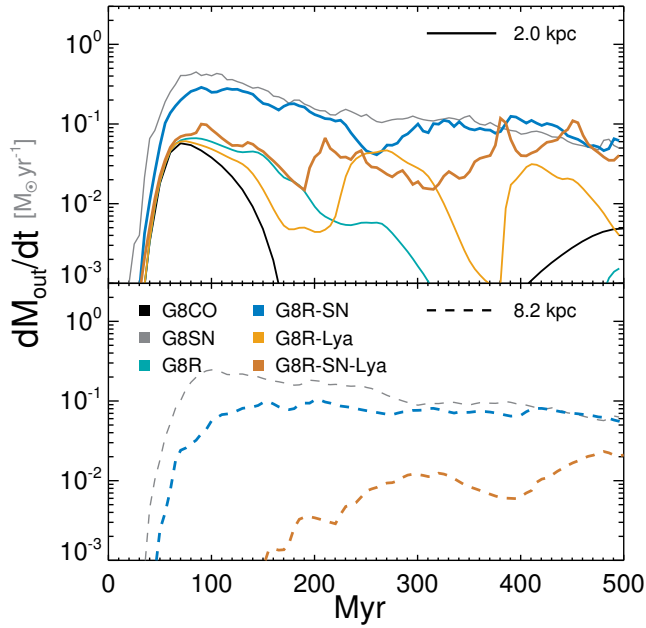
Figure 7. Galactic outflow rates measured at two different heights ($|z| = 2\,$kpc; top panel, $|z| = 8.2\,$kpc: bottom panel). Different models are shown as different colour-codings, as indicated in the legend. The models with weak feedback (NoFB, R, and R-Lya) cannot launch strong outflows that reach $0.2\,R_{\rm vir} (= 8.2\,$kpc), and thus does not appear in the bottom panel.
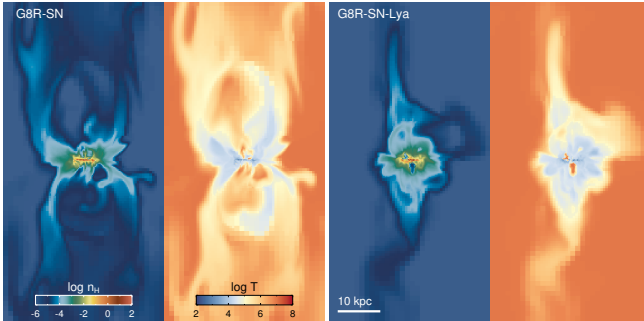

Figure 8. Slices of density and temperature distributions from the two runs (G8R-SN: left, G8R-SN-Lya: right) at $t = 500\,$Myr. Each plot measures $37.5\,$kpc $\times\,75\,$kpc.

drive fast, mass-conserving winds that propagate out to the CGM. At $t = 500\,$Myr, a bipolar outflow extends to the virial radius of the dark matter halo $\sim 40\,$kpc (Figure 8). Surprisingly, we find that the addition of Lyα pressure leads to weaker outflows than G8R-SN. Even though the two runs sometimes display comparable outflow rates in the inner region ($|z| = 2\,$kpc), the large-scale bipolar outflows are not observed in the run with Lyα pressure.

To better understand the properties of outflows from these simulations, we measure the mass-loading factors, the typical density, velocity, and temperature of the outflows responsible for most of outflowing mass in Figure 9. To do this, we average the latter quantities by weighting the mass flux ($\rho v_r \Delta x^2$). To estimate the mass-loading factor, we use the star formation rates averaged over 50 Myr, as the instantaneous rates vary widely in time. Several interesting features can be inferred from this plot. First, the mass-
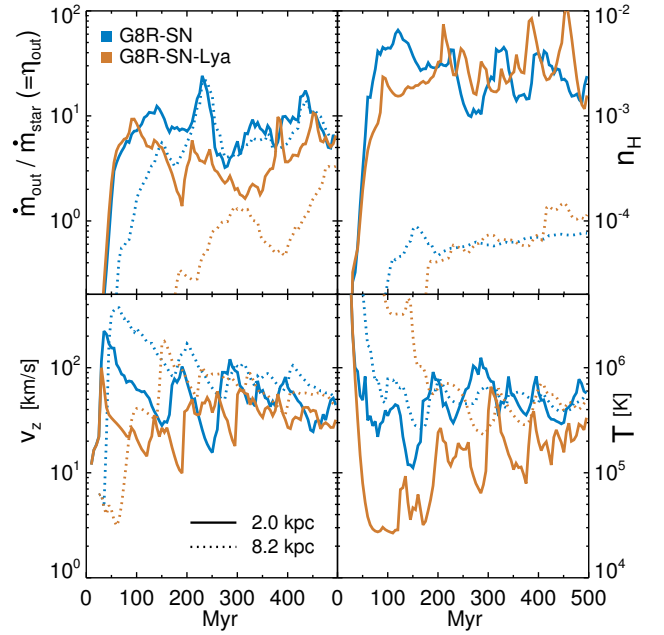

Figure 9. Properties of the galactic outflows in the runs without (G8R-SN) and with Lyα pressure (G8R-SN-Lya). From the top left, each panel shows the outflow rates in M$_\odot$ yr^{-1}, flux-averaged density in cm^{-3}, outflow velocities in km s^{-1}, and temperature in Kelvin. The solid lines denote the properties measured at $|z| = 2\,$kpc, whereas the properties measured at $|z| = 8.2\,$kpc are shown as the dotted lines. Outflows tend to be slower and cooler in the run with Lyα pressure.

loading factor in the G8R-SN run is larger than G8R-SN-Lya. The time average of the mass-loading factor measured at $|z| = 2\,$kpc during a settled period ($300 \le t \le 500\,$Myr) is $\eta_{\rm out} = 8.0^{+3.1}_{-2.2}$ and $4.0^{+2.9}_{-1.7}$ in the G8R-SN and G8R-SN-Lya run, respectively. Note that the mass loading without Lyα photons (G8R-SN) is broadly consistent with the independent work by Hu et al. (2017). The difference in the mass-loading between the two models becomes more pronounced if we compare the loading factors at $8.2\,$kpc ($= 0.2\,R_{\rm vir}$) ($\eta_{\rm out} = 6.8$ vs 1.0). This is indicative that the powerful outflows seen in the SN run is not solely due to higher *average* star formation rates.

The velocity of the outflows in the inner region of the galaxy tends to be faster in the run without Lyα[5], compared to the fiducial run. The inner galactic winds often have $v_z \gtrsim 100\,$km s^{-1}, which is larger than the escape velocity of the halo ($v_{\rm esc} \sim 40\,$km s^{-1}). On the other hand, a more gentle velocity of $v_z \sim 20$–$60\,$km s^{-1} is seen in our preferred model (G8R-SN-Lya). Similarly, the temperature of the inner outflows is also cooler in the run with Lyα ($T \sim 0.5 \times 10^5 - 3 \times 10^5\,$K), even though the typical density responsible for the outflows are comparable. As the winds propagate outwards, some of the component with low velocity falls back and does not contribute to the outflows in the outer region of the halo, leading to the slight increase in velocity at $r = 0.2\,R_{\rm vir}$. This is notable in the G8R-SN-Lya run where the temperature of the outflows is increased to $\sim 4 \times 10^5\,$K in the outer region of the halo.

---

[5] Note that the outflow velocity in the run with Lyα could increase further if the gas were irradiated by a non-thermal Compton-thick spectrum from massive black holes, as the harder spectrum allows for neutral hydrogen to survive longer than the normal Pop II spectrum (Smith et al. 2016).
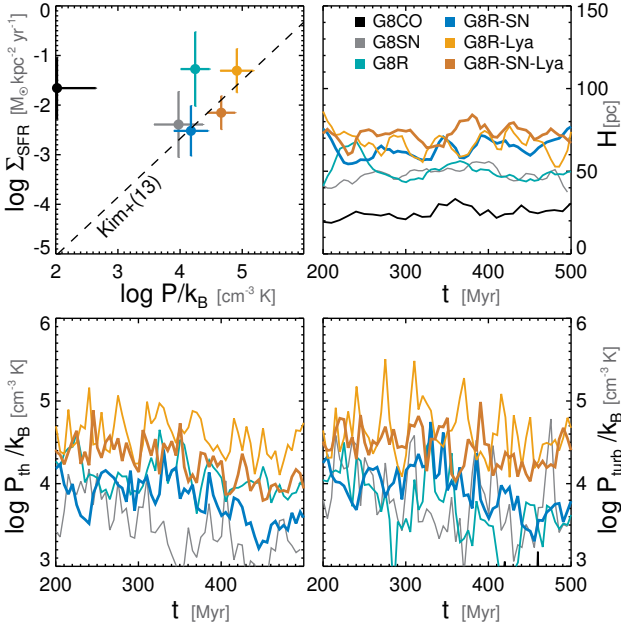
Figure 10. Effects of different feedback processes on the vertical structure of the ISM. The top left panel shows the relationship between the total pressure (turbulent + thermal) and the star formation rate density (Σ_{SFR}). The dashed line displays the fit to the results from local shearing box simulations by Kim et al. (2013). The top right, bottom left, and bottom right panel presents the time evolution of the scale-height of the gaseous disk, thermal pressure, and turbulent pressure in the mid plane ($|z| \leq H$). It can be seen that the disk becomes thicker in the run with Lyα feedback (R-SN-Lya) than the run without it (R-SN).

We also find that the density of the winds varies substantially as a function of radius. The density of the outflows at $|z| = 2\,\mathrm{kpc}$ is $n_{\mathrm{H}} \sim 0.003\,\mathrm{cm}^{-3}$, while it is reduced by more than an order of magnitude at $|z| = 8.2\,\mathrm{kpc}$. We mainly attribute this to the fact that the internal pressure of the outflows ($P/k_B \sim 10^3\,\mathrm{cm}^{-3}\,\mathrm{K}$) is larger than the pressure in the ambient medium ($P/k_B = 10\,\mathrm{cm}^{-3}\,\mathrm{K}$). For comparison, the ram pressure exerted by the halo gas is negligible for the initial conditions chosen ($P_{\mathrm{ram}}/k_B \sim 1\,\mathrm{cm}^{-3}\,\mathrm{K}$). Thus, the reduction in density is likely caused by adiabatic expansion. However, we note that our refinement strategy may also be partially responsible for the lower density. Since refinement is triggered based on mass and jeans length (i.e. not on pressure), computational grids are split slower than the propagation of outflows, which may have resulted in more diffuse structures that it should.

3.3 Structure of the Interstellar medium

Small-scale simulations demonstrate that feedback from SNe is essential to provide vertical support against gravity in the ISM (deAvillez & Breitschwerdt 2005; Joung et al. 2009b; Hill et al. 2012; Kim et al. 2013; Walch et al. 2015), possibly explaining the development of the internal turbulent structure inside molecular clouds (Padoan et al. 2016). For example, Kim et al. (2013) showed using a set of shearing box simulations that the stratified medium can be in vertical dynamical equilibrium if SN explosions are placed in dense regions ($n_{\mathrm{H}} \gtrsim 100\,\mathrm{cm}^{-3}$). The authors argue that the turbulent motions that develop due to SNe provide a factor of a few

larger pressure than the thermal support. In this section, we study the effects of different feedback processes on the vertical structure of the ISM.

Following Kim et al. (2013), we compute the scale-height as $H = \sqrt{\int \rho z^2 dV / \int \rho dV}$, where the integration is done over the gas within the scale-length of the gaseous disk in the $x-y$ plane and $|z| \leq 250\,\mathrm{pc}$. The turbulent and thermal pressure within the scale-length of the disk at the mid plane ($|z| \leq H$) is then calculated as

$$P_{\mathrm{th}} = \int P\Theta(n_{\mathrm{H}} < n_{\mathrm{GBC}})dV / \int \Theta(n_{\mathrm{H}} < n_{\mathrm{GBC}})dV, \quad (21)$$

$$P_{\mathrm{turb}} = \int \rho v_z^2 \Theta(n_{\mathrm{H}} < n_{\mathrm{GBC}})dV / \int \Theta(n_{\mathrm{H}} < n_{\mathrm{GBC}})dV, \quad (22)$$

where $n_{\mathrm{GBC}} \approx 50\,\mathrm{cm}^{-3}$ is the density of a gravitationally bound cloud above which gas is dense enough to self-gravitate, and Θ is the Heaviside step function.

Figure 10 shows that the disk becomes thicker by adding more energy from various feedback sources. The disk scale-height is barely resolved in the run without feedback ($H \sim 20 - 30\,\mathrm{pc}$), as the thermal and turbulent pressure are very low ($\langle P/k_B \rangle \sim 100\,\mathrm{cm}^{-3}\,\mathrm{K}$). The inclusion of photoionization heating increases the thermal pressure substantially ($\langle P_{\mathrm{th}}/k_B \rangle \sim 10^{4.1}\,\mathrm{cm}^{-3}\,\mathrm{K}$), resulting in a thicker disk ($\langle H \rangle \approx 51\,\mathrm{pc}$) (see also Rosdahl et al. 2015). The turbulent pressure is also increased ($\langle P_{\mathrm{turb}}/k_B \rangle \sim 10^{3.7}\,\mathrm{cm}^{-3}\,\mathrm{K}$), although it is smaller than P_{th} by a factor of two. The turbulent pressure becomes stronger (by $\sim 30\%$) than the thermal pressure when SNe inject the kinetic energy into the ISM (G8R-SN), leading to $\langle H \rangle \approx 64\,\mathrm{pc}$. Ly$\alpha$ feedback further thickens the disk ($\langle H \rangle \approx 73\,\mathrm{pc}$), as both thermal and turbulent pressures are enhanced. Note that the mass-weighted average density of the diffuse component in the mid plane is roughly a factor of four larger ($\langle n_{\mathrm{H},0} \rangle \approx 8\,\mathrm{cm}^{-3}$) in the G8R-SN-Lya model, compared to that in G8R-SN ($\langle n_{\mathrm{H},0} \rangle \approx 2\,\mathrm{cm}^{-3}$), due to the less bursty star formation. The run with Lyα only (G8R-Lya) exhibits the highest pressure, as the local radiation field is intense owing to the less efficient regulation of star formation.

The top left panel of Figure 10 suggests that our simulated galaxies with SN feedback are in approximate pressure equilibrium. The thermal and turbulent pressure remain around $P/k_B \sim 10^4 - 10^5\,\mathrm{cm}^{-3}\,\mathrm{K}$, which is similar to the pressure required to counter-balance vertical weight of the ISM ($\approx 10^4\,\mathrm{cm}^{-3}\,\mathrm{K}(\Sigma/10\,\mathrm{M}_\odot\,\mathrm{pc}^{-2})\sqrt{\rho_{\mathrm{sd}}/0.1\,\mathrm{M}_\odot\,\mathrm{pc}^{-3}}$), where $\Sigma \approx 20 - 30\,\mathrm{M}_\odot\,\mathrm{pc}^{-2}$ is the gas surface density, and $\rho_{\mathrm{sd}} \approx 0.1 - 0.2\,\mathrm{M}_\odot\,\mathrm{pc}^{-3}$ is the mid-plane density due to stars and dark matter (Ostriker et al. 2010; Kim et al. 2013). The two models (G8R-SN and G8R-SN-Lya) are also in good agreement with the fitting results from the local shearing box simulations (Kim et al. 2013) where the ISM is shown to be in vertical equilibrium. The main difference is that turbulent support in our simulations does not appear to contribute substantially to the total pressure as in Kim et al. (2013). For example, their gas-rich ($\Sigma = 20\,\mathrm{M}_\odot\,\mathrm{pc}^{-2}$) models (QA20 series), which is comparable to our conditions ($\langle \Sigma \rangle \approx 33\,\mathrm{M}_\odot\,\mathrm{pc}^{-2}$), exhibit a factor of 2–3 larger turbulent support than thermal pressure, but we found that the turbulent pressure is stronger than thermal pressure only by $\sim 50\%$. We attribute this to the fact that photo-ionization heating provides a extra thermal pressure to the diffuse gas in the mid plane. Indeed, when we do not consider any type of radiation feedback (G8SN), the turbulent support is found to be roughly twice as strong as the thermal support (see also Kim et al. 2013). As a result, the disk thickness in this run ($\langle H \rangle \sim 48\,\mathrm{pc}$) is smaller than in the run with radiation.
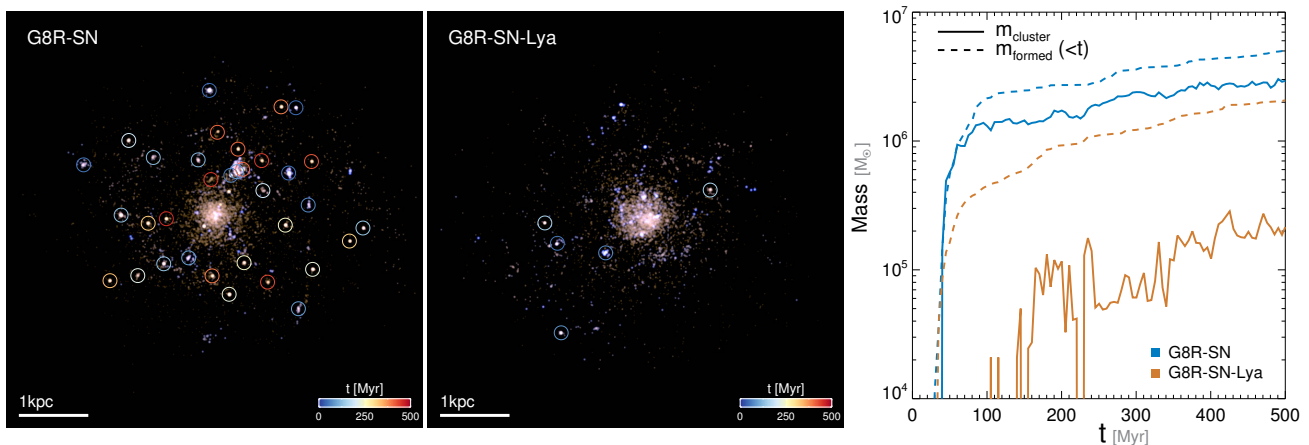
Figure 11. Star clusters in the run without and with Lyα pressure. The composite image is made using the GALEX NUV, SDSS g, and i bands. The circles denote the position of star clusters identified using the hierarchical clustering algorithm (HDBscan). The mean age of each star cluster is shown using different colour-codings, as indicated in the legend. The rightmost panel presents the mass enclosed within star clusters outside 0.5 kpc as a function of time (soild lines) and the integrated stellar mass formed at $r \geq 0.5$ kpc (dashed lines). Note that the majority ($\sim 90\%$) of star particles do not belong to any star clusters in the G8R-SN-Lya run, whereas $\sim 50\%$ of the mass is locked up in star clusters in G8R-SN.

3.4 Formation of massive star clusters

Given the large multiplication factor of Lyα photons in the metal-poor environment, the relative difference in stellar mass between G8R-SN and G8R-SN-Lya may not appear very remarkable. However, Figure 11 demonstrates that Lyα feedback plays a crucial role in shaping the formation of star clusters. To quantitatively measure this, we use a hierarchical clustering algorithm based on the mutual reachability distance, HDBscan[6] (Campello et al. 2013). The algorithm generates the member list of each cluster without assuming any particular structure. We determine the centre by iteratively computing the centre of mass within a fixed 100 pc radius. A cluster with fewer than 20 particles or a structure that is not centrally well concentrated (i.e., $M_{\rm star}^{\rm r<50pc}/M_{\rm star}^{\rm r<100pc} > 0.5$) is removed from the cluster list.

The number of star clusters present in the final snapshot ($t = 500$ Myr) is 34 in G8R-SN, whereas only 5 clusters are identified in the fiducial run. Note that we ignore any clusters located in the inner region ($r < 0.5$ kpc), because we are mainly interested in the survivability of star clusters against internal feedback processes. The final mass contained in the star clusters outside 0.5 kpc in the G8R-SN and G8R-SN-Lya run is 2.3×10^6 M$_\odot$ (35.3% of the total stellar mass) and 1.7×10^5 M$_\odot$ (4.4%), respectively. Individual star clusters are also less massive in the run with Lyα feedback. The typical mass of a star cluster found in the simulations is 5.1×10^4 M$_\odot$ and 2.6×10^4 M$_\odot$, respectively.

Figure 11 also shows that Lyα pressure makes massive star clusters more difficult to form and survive. The rightmost panel displays the integrated mass of stars formed outside 0.5 kpc (dashed lines) and the mass enclosed within clusters as a function of time. Here we combine the initial mass of star particles for the enclosed mass instead of actual particle mass at time t in order to directly compare with the stellar mass formed. There are considerably more old star clusters in the G8R-SN run, while only young star clusters are left in G8R-SN-Lya (see the colour of the circles). It is also evident from this plot that a large fraction of stars ($\sim 90\%$) do not belong to any star cluster in the G8R-SN-Lya run. This indicates that

Lyα pressure regulates the efficiency for an individual star formation event from the early stage of cluster formation. It is also likely that small clusters are formed and then dispersed as early feedback processes blow away the self-gravitating gas through non-adiabatic expansion (Pontzen & Governato 2012; Teyssier et al. 2013). The rapid variation of the mass enclosed within star clusters corroborates that star clusters are short-lived in the presence of strong early feedback. On the contrary, G8R-SN appears to convert the gas into stars more efficiently, turning them into a self-gravitating object. As a result, a large fraction of star clusters ($\sim 50\%$) survive SN explosions.

Some authors claim that globular clusters (GCs) may form in the gas-rich galactic disc (e.g. Kravtsov & Gnedin 2005), and one may wonder how the star clusters identified from our simulations compare with the properties of GCs. Since the half-mass radii of the clusters are barely resolved in our simulations (≈ 14 pc), we focus on the age and mass. The simulated star clusters are less massive than the GCs ($\sim 10^5$ M$_\odot$) by a factor of a few, and show significant internal age dispersions, 6 Myr (R-SN-Lya) or 24 Myr (R-SN), respectively. The maximum mass of the clusters (3.0×10^5 M$_\odot$ and 8.9×10^4 M$_\odot$ in the run without and with Lyα pressure) is also smaller than what is typically derived in observations ($\sim 10^6$ M$_\odot$). More importantly, the short lifetimes of the star clusters in the G8R-SN-Lya run do not seem to favour the scenario in which GCs form inside a metal-poor, gas-rich disk, and survive to the present day. We note, however, that the observed specific frequency of the GCs in dwarf galaxies comparable to our simulated one ($L_V \sim -14$) ranges from 0 to 5 (e.g., Georgiev et al. 2010), and thus the short lifetimes do not necessarily rule out the general possibility of forming a GC in gas-rich, massive spiral galaxies.

Our experiments demonstrate that Lyα pressure may be a critical mechanism by which potential globular cluster candidates with low metallicities are disrupted. Even if the mechanism cannot disrupt a GC, it may help to suppress the internal age and metallicity dispersions of the clusters by truncating star formation early on (e.g. Kimm et al. 2016). In this regard, future simulations aiming to understand the detailed formation histories of metal-poor GCs may
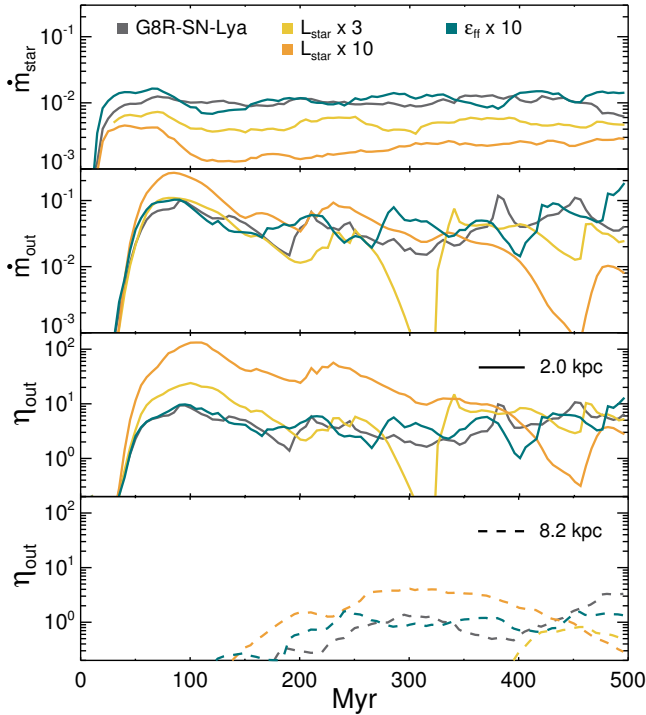
[6] http://hdbscan.readthedocs.io/en/latest/index.html

Figure 12. Effects of the different radiation field strength and star formation efficiency. The models in which the luminosity of stars is boosted by a factor of 3 (`G8R-SN-Lya-f3`) or 10 (`G8R-SN-Lya-f10`) are shown as yellow and red colours, respectively. The blue lines show the case in which $\epsilon_{\rm ff}$ is boosted by an order of magnitude (`G8R-SN-Lya-s10`). From top to bottom, each panel displays the star formation rates, outflowing rates, mass-loading factors ($\eta_{\rm out}$) measured at $|z| = 2$ kpc, and $\eta_{\rm out}$ measured at $0.2\,R_{\rm vir} = 8.2$ kpc. Note that $\eta_{\rm out}$ at $0.2\,R_{\rm vir}$ is smaller than ~ 10 even with extreme feedback (`G8R-SN-Lya-f10`).

need to include Lyα feedback along with other radiation feedback processes.

4 DISCUSSION

4.1 Effects of early stellar feedback

We have demonstrated in the previous section that the inclusion of Lyα pressure disrupts gas clouds more efficiently than the run without it. Nevertheless, the mass-loading factors are decreased, compared to the run without Lyα feedback, as star formation becomes less bursty and SNe do not explode in a collective manner. This raises the question as to whether or not early stellar feedback can help drive strong winds that carry a large amount of gas in low-mass haloes (e.g. Muratov et al. 2015). To investigate this, we run two additional simulations by artificially increasing the luminosity of individual stars by a factor of 3 (`G8R-SN-Lya-f3`) or 10 (`G8R-SN-Lya-f10`). By doing so, we enhance not only the pressure from multi-scattered Lyα photons but also photo-ionization heating and radiation pressure from UV and IR, although the most significant impact still originates from Lyα feedback. Note that the inclusion of higher mass stars in a simple stellar population up to $M_{\rm max} = 300\,{\rm M}_\odot$, as opposed to $M_{\rm max} = 100\,{\rm M}_\odot$, can easily boost the number of ionizing photons by a factor of ≈ 2. In this regard, `G8R-SN-Lya-f3` may be taken as the optimistic but still
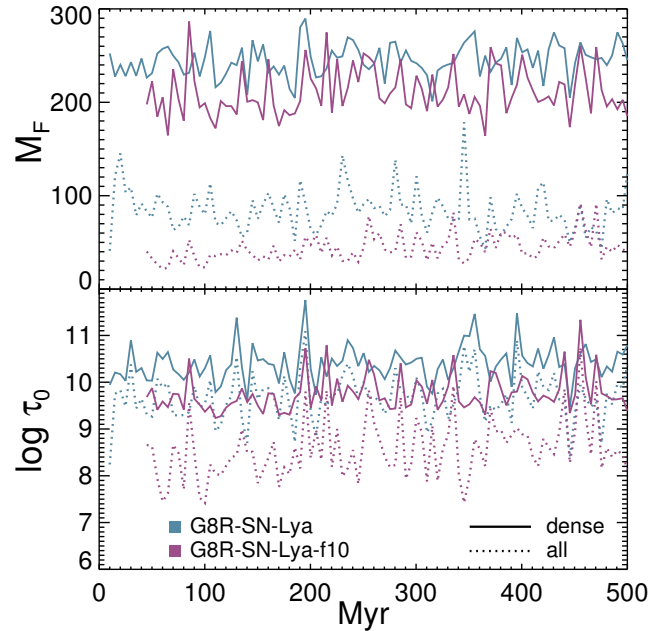

Figure 13. The photon number ($N_{\rm Lya}$)-weighted average of the multiplication factors (top panel) and optical depths to Lyα photons at the line centre (bottom panel). The solid lines show M_F and τ_0 of the dense regions ($n_{\rm H} \geq 100\,{\rm cm}^{-3}$), whereas the dotted lines show the average for the entire gas. The blue and violet colours indicate the runs with the normal and extreme radiation field.

plausible model. However, `G8R-SN-Lya-f10` is certainly an extreme case, which may be used to learn about the effects of early feedback.

Figure 12 shows that star formation rates are directly affected by the strength of radiation field from stars in the presence of Lyα pressure. The total amount of stars formed during 500 Myr is reduced by a factor of ≈ 2 or 4 in the runs with three times or ten times more photons ($2.4 \times 10^6\,{\rm M}_\odot$ and $1.2 \times 10^6\,{\rm M}_\odot$ for the `f3` and `f10` runs, respectively). Note that the suppression of star formation is not simply proportional to the boost factor. This is partly because Lyα photons cannot reside in an extremely optically thick region for a long time if star-forming clouds are irradiated by intense radiation. Figure 13 substantiates this by showing that the $N_{\rm Lya}$-weighted mean multiplication factor is systematically reduced from $\langle M_F \rangle = 244$ to 212 in dense regions ($n_{\rm H} \geq 100\,{\rm cm}^{-3}$). The difference is more noticeable in the less dense environments ($n_{\rm H} < 100\,{\rm cm}^{-3}$, $\langle M_F \rangle = 91.2$ vs 47.6), meaning that the ISM becomes more diffuse under strong radiation feedback. Figure 13 (bottom panel) indeed shows that the optical depth to Lyα photons at the line centre is decreased by an order of magnitude around young stars.

Outflow rates are adjusted in such a way that the mass loading factors measured at $|z| = 2$ kpc are around 2–10 between $300 \leq t \leq 500$ Myr. The extreme model displays $\eta_{\rm out}$ up to ~ 100 in the initial phase during which the mean density of the outflow is temporarily augmented by a factor of two and the covering fraction of the outflows is increased by a factor of five. However, the velocity ($10 - 30\,{\rm km\,s}^{-1}$) and temperature ($T \sim 10^5$ K) of the outflows are largely unchanged despite the significant decrease in star formation rates. The condition for such a gas-rich environment may be met during the starburst phase (e.g. merg-

ers). Even when radiation feedback is artificially boosted by an order of magnitude, the mass loading factor measured at $0.2\,R_{\rm vir}$, especially at late times, turns out to be remarkably smaller than previous studies which successfully reproduce a variety of observations (see also Rosdahl et al. 2015). For example, Muratov et al. (2015) obtained $\eta_{\rm out} \sim 40 - 100$ with the median velocity of $v_{\rm wind} \sim 40 - 80\,{\rm km\,s^{-1}}$ in halos of mass adopted in this study. The momentum-driven wind model by Oppenheimer & Davé (2008) used a more similar mass loading ($\eta_{\rm out} \approx 5$ if we assume $\sigma \approx V_c/\sqrt{2}$), although the wind velocity at the time of injection is slightly higher than our predictions.

One of the main differences from the simulations used in Muratov et al. (2015) is the way star formation is modelled. Although the idea behind the use of local gravity is very similar, the efficiency for star formation per free-fall time is set to 100% in the FIRE simulation (Hopkins et al. 2014), while the typical efficiency is 16% in the G8R-SN-Lya run. Although $\epsilon_{\rm ff} = 16.4\%$ is still higher than what we find on galactic scales in the local Universe (Kennicutt 1998; Evans et al. 2014), the finite resolution of our simulations may require even a higher efficiency to take the best advantage of clustered SN explosions. Motivated by this, we also test a model in which $\epsilon_{\rm ff}$ is boosted by an order of magnitude (G8R-SN-Lya-s10). Because adding extra pressure in star-forming regions from radiation feedback usually reduces $\epsilon_{\rm ff}$, we find that the resulting $\epsilon_{\rm ff} = 1.37$ is slightly smaller than 1.64 ($10 \times \epsilon_{\rm ff}$ from G8R-SN-Lya), but still significantly higher than the fiducial run. Figure 12 shows that the models yield very similar results not only in terms of star formation rates but also in outflow rates. We find that the properties of the outflows are also indistinguishable between the enhanced $\epsilon_{\rm ff}$ model and the fiducial model, although the escape fractions of LyC photons are increased (see the next section). This is again due to the fact that Lyα pressure controls the dynamics of star-forming clouds and suppresses very bursty star formation episodes.

To summarise, these extreme models demonstrate that strong early feedback does not necessarily enhance outflow rates, but mostly acts to stabilise the star formation histories of the galaxy, reducing the mass-loading factor. This calls into question how gas can be entrained at truly enormous mass loading factors ($\eta_{\rm out} \sim$ 50–100). Unfortunately, there are only a handful of local analogues of high-z dwarf galaxies. Furthermore, making a direct comparison to these observations is not straightforward. Heckman et al. (2015) shows that dwarf galaxies with circular velocities of $v_{\rm cir} \sim 40\,{\rm km\,s^{-1}}$ tend to show intermediate mass loadings of $\dot{M}_{\rm out}/\dot{M}_\star \sim 6 - 8$, but these systems appear to have larger stellar masses and star formation rates ($\dot{M}_\star \sim 0.1\,{\rm M_\odot\,yr^{-1}}$). The most relevant sample from Heckman et al. (2015) is I Zw 18, which has a very similar metallicity and star-formation rate as our simulated galaxies, but only an upper limit on the mass loading of $\dot{M}_{\rm out}/\dot{M}_\star < 60$ is placed due to the ambiguity of outflow velocities ($v_{\rm out}$). Moreover, it should be noted that these estimates are computed by counting all the mass along the line of sight ($N_{\rm out} \langle m \rangle$) and assuming that outflows are launched at twice the starburst radius ($r_{\rm out} \sim 2\,r_\star$), i.e. $\dot{m}_{\rm out} = 4\pi N_{\rm out} \langle m \rangle v_{\rm out} 2\,r_\star$, where $N_{\rm out}$ is the column density of the outflow, and $\langle m \rangle$ is the mean mass per particle. Since the outflow rates can be written as $\dot{m}_{\rm out}(r) = 4\pi r^2 \rho v_r$, the above equation implicitly assumes that the surface density is $\Sigma = N_{\rm out} \langle m \rangle \sim r_{\rm out} \rho(r_{\rm out})$. For outflowing gas that follows an isothermal profile[7] with a truncation radius

at a, $\rho = A/(r^2 + a^2)$, one can show that the integrated surface density from the centre to a radius R is $\Sigma(\le r) = \frac{A}{a}\tan^{-1}\left(\frac{r}{a}\right)$, where $A = \frac{M_{\rm out}}{4\pi\left(R_{\rm vir} - \tan^{-1}[R_{\rm vir}/a]\right)}$. Thus, the integrated surface density, $\Sigma(< R_{\rm vir}) \sim N_{\rm out} \langle m \rangle$, used in the observation to derive outflow rates is likely to be larger than $r_{\rm out}\rho(r_{\rm out})$ by 3–4 times for $r_\star \le a \le 3r_\star$, and any discrepancy (or agreement) between observations and simulations should be taken with caution. Of course, if the outflows are not mass conserving (e.g. Leroy et al. 2015), the discrepancy would be smaller. Recent work by Chisholm et al. (2017) takes into account this possibility along with the photoionization on ultraviolet spectra from the Cosmic Origin Spectrograph on the Hubble Space Telescope, and conclude that the *maximum* mass loading factors of the systems (SBS 1415+437 and I Zw 18) that share a similar star formation rate ($0.02\,{\rm M_\odot\,yr^{-1}}$) are 19 ± 17 and 11 ± 8.0, respectively. Intriguingly, the mass-loading from our fiducial model does not seem in stark contradiction to these estimates. However, in order to draw a firm conclusion, it will be necessary to generate mock absorption spectra and re-derive the mass loading based on the same methodology used in observations.

4.2 Possible implications for reionisation

Studies show that the disruption of star-forming clouds is crucial for ionizing photons to escape from their host dark matter haloes and reionize the Universe (Wise & Cen 2009; Dale et al. 2012; Kimm & Cen 2014; Wise et al. 2014; Paardekooper et al. 2015; Kimm et al. 2017; Trebitsch et al. 2017). Given that Lyα feedback accelerates the disruption process, it is necessary to check whether or not the mechanism may change the previous picture of reionization. To investigate this in detail, we measure escape fractions by computing the escaping probability of LyC photons on the virial sphere of the dark matter halo as follows. We use the HEALPIX algorithm (Górski et al. 2005) to generate 2048 photons per star particle, which carries information about a spectral energy distribution as a function of wavelength for a given age, mass, and metallicity. The photons are attenuated by neutral hydrogen, as $f_{\rm abs}(\nu) = f_{\rm int}(\nu)\exp\left[-\tau_{\rm HI}(\nu)\right]$, where $\tau_{\rm HI} (= N_{\rm HI}\sigma_{\rm HI})$ is the optical depth and $\sigma_{\rm HI}$ is the hydrogen absorption cross section (Osterbrock & Ferland 2006). We also take into account the small magellanic cloud-type dust (Weingartner & Draine 2001), but its contribution turns out to be negligible even with the high dust-to-metal ratio of 0.4.

The left panel of Figure 14 presents the instantaneous (dotted lines) and photon-number weighted average escape fractions (solid lines) of the two most interesting runs (G8R-SN and G8R-SN-Lya) at $200 < t < 500$ Myr. We do not include the initial phase of gas collapse, because the ISM structures are likely to be affected by the initial condition, although including the results does not change any of the conclusions that follow. The figure also includes the photon production rates in the bottom left panel, and one can see that the escape fractions tend to be higher after strong starburst, which is consistent with previous findings from cosmological RHD simulations (Kimm & Cen 2014; Wise et al. 2014; Kimm et al. 2017; Trebitsch et al. 2017).

Interestingly, we find that a slightly smaller fraction of the ionizing photons escapes from the dark matter halo in the run with Lyα feedback. The photon-number weighted average escape fractions at $200 < t < 500$ Myr are measured to be $\langle f_{\rm esc,LyC} \rangle =$

---

[7]   Muratov et al. (2015) shows that the outflowing mass contained in

equally binned shells in dwarf-sized halos is more or less constant, indicative of $\rho \propto r^{-2}$.
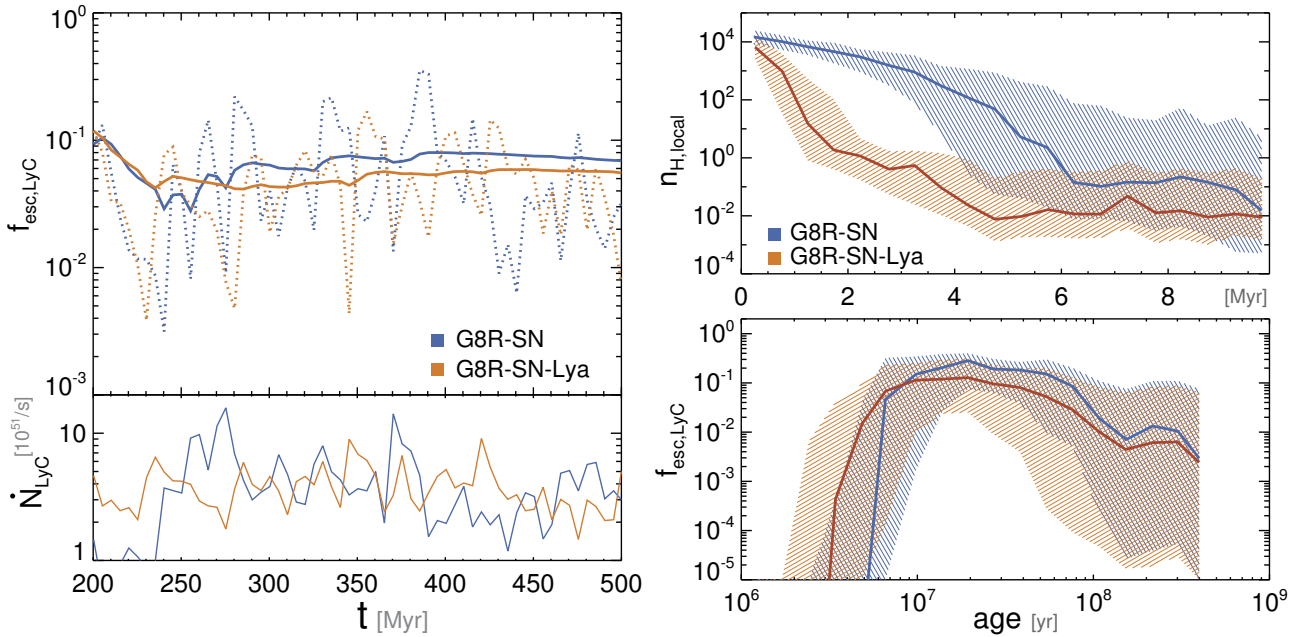
Figure 14. *Left*: Escape fractions and production rates of LyC photons in two different runs. The dotted and solid lines show the instantaneous and photon-number averaged $f_{\rm esc,LyC}$. *Right*: the local density in which star particles with different ages are located (top) and the median instantaneous $f_{\rm esc,LyC}$ as a function of the age of star particles. The shaded regions mark the interquartile range of the distributions. Although Lyα feedback lowers the density around young stellar populations, the average escape fractions turn out to be smaller than those from the G8R-SN run (see the text).
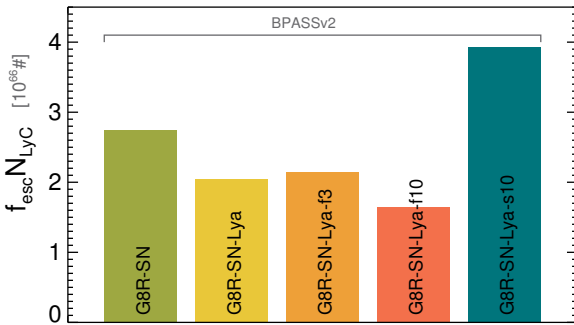
Figure 15. The integrated number of escaping LyC photons in the simulations with various feedback strength between $200 \leq t \leq 500\,{\rm Myr}$. It can be seen that the number of escaping photons are not very sensitive to the strength of radiation feedback, but it depends more on the star formation model.

5.5% and $\langle f_{\rm esc,LyC} \rangle = 6.9\%$ for the runs with and without Lyα feedback, respectively. This is somewhat counter-intuitive, given that the inclusion of early feedback is expected to lower the local gas density surrounding stars. The right panel of Figure 14 indeed demonstrates that the gas density of the cells in which star particles older than $\sim 2\,{\rm Myr}$ live is $n_{\rm H} \lesssim 1\,{\rm cm}^{-3}$, which is much lower than the G8R-SN case. These cells are sufficiently diffuse to become ionized by a single star particle of mass $910\,{\rm M}_\odot$, and we also confirm that the ionization fraction of the cells hosting stars older than $\sim 2\,{\rm Myr}$ in the G8R-SN-Lya run is close to unity.

The lower escape fractions in the G8R-SN-Lya run can be understood in terms of the efficiency of creating channels transparent to LyC photons. Kimm et al. (2017) show that the escape fractions can be as high as $f_{\rm esc,LyC} \sim 40\%$ if a large number of stars are formed instantaneously and the birth clouds are dis-

rupted by photo-ionization heating. However, if the cloud is massive enough to delay and confine the propagation of ionizing radiation within the galactic ISM, the escape fractions are unlikely to be high. Figure 14 (right panel) supports this claim by showing that $f_{\rm esc,LyC}$ of stars younger than $t \sim 10\,{\rm Myr}$ is very low[8]. On the contrary, stars older than $t \sim 10 - 100\,{\rm Myr}$ exhibit a higher $f_{\rm esc,LyC}$ of $\sim 10 - 30\%$. The fact that G8R-SN displays a higher average $f_{\rm esc,LyC}$ in these stars suggests that more coherent Type II SNe from bursty star formation are better at creating HII holes than Lyα pressure, as the latter is a gentle process that does not drive extended outflows. Stars older than 100 Myr exhibit lower escape fractions again, because they cannot emit a large number of LyC photons and the resulting Stromgren sphere is very small.

However, when radiation pressure by Lyα photons dominates over the effects due to SNe, the escape fractions of ionizing radiation are increased significantly. For the runs employing a stronger radiation field (G8R-SN-Lya-f3), 11.6% of ionizing photons leak out from the dark matter halo. The escape fraction is further increased to 18.5% in the G8R-SN-Lya-f10 run.

The balance between enhanced escape fractions and reduced star formation implies that the reionization history of the Universe may not be significantly affected by the presence of Lyα feedback. Figure 15 shows that the integrated number of escaping LyC photons in the plausible models (R-SN, R-SN-Lya, R-SN-Lya-f3) is reasonably similar. Even the extreme feedback model produces a mere 20% fewer escaping photons than those from R-SN-Lya. In a slightly different context, Kimm & Cen (2014) also report that a similar number of LyC photons escapes from dark matter halos ir-

---

[8] Note that since the outer region of the simulated halo is hot, all of the absorption takes place within the galaxy, and any photons that leave the galaxy can easily reach the virial radius.

respective of the presence of runaway stars, because runaway stars suppress star formation but enhance escape fractions.

However, we find that the predicted escape fractions rely on the choice of the star formation model. In the `G8R-SN-Lya-s10` case where star formation is designed to be locally more bursty, radiation feedback comes into play earlier than in the case of `G8R-SN-Lya`, lowering the local densities of young stars ($\lesssim 5\,\mathrm{Myr}$) even further than the fiducial model. As a result, $\langle f_{\mathrm{esc,LyC}} \rangle$ is elevated to 8.8%, which is roughly twice larger than the fiducial case despite the fact that a similar amount of stars is formed in both runs. Even though we prefer our star formation model in which the efficiency per free-fall time is calculated based on the local virial parameter and turbulence, the uncertainty is still worrisome, and will be required to test against well resolved, cloud simulations (e.g. Dale et al. 2012; Geen et al. 2016; Gavagnin et al. 2017).

4.3 Caveats

We emphasise that there are several important caveats in the modelling of Lyα feedback. First, the amount of dust in high-z metal-poor galaxies is highly uncertain. We adopt the values derived from the local dwarf galaxies (Rémy-Ruyer et al. 2014), but these estimates are still uncertain due to small number statistics. Nonetheless, there is a clear indication that the relative mass fraction of dust with respect to metal mass is much smaller than those of local spiral galaxies (Lisenfeld & Ferrara 1998; Engelbracht et al. 2008; Galametz et al. 2011; Fisher et al. 2013; Rémy-Ruyer et al. 2014). If we assume that the dust-to-metal ratio is only 20 times smaller than the local solar neighbourhood (i.e. $f_{\mathrm{d/m}} = 0.05$), instead of $f_{\mathrm{d/m}} = 0.005$ we adopt in this study, the maximum multiplication factor will decrease from $M_{F,\mathrm{max}} = 355$ to $M_{F,\mathrm{max}} = 216$. This will give similar effects as decreasing the luminosity of stars by $\approx 40\%$. However, given that the number of ionizing photons from a simple stellar population can be augmented by a factor of two when the formation of massive stars ($M \geq 100\,\mathrm{M_\odot}$) is allowed, the effects due to Lyα scattering are not probably severely over-estimated.

Second, even though the radial momentum from Lyα pressure is estimated based on a Monte Carlo Lyα radiative transfer code (RASCAS), our subgrid model cannot account for the long range force due to spatially diffused Lyα photons after scattering. Such a calculation would require fully coupled radiative transfer, as in Smith et al. (2017b,a), but this is not yet feasible for three dimensional galactic-scale simulations[9]. As a first step, we focus on the short-range force that primarily affects the evolution of star-forming clouds. Note that this is a reasonable approximation, as long as the majority of Lyα photons are destroyed by dust inside the GMC. Indeed, as shown in Figure 13, the multiplication factors from `G8R-SN-Lya` are already close to the maximum value one can exploit from the metal-poor environments ($M_{F,\mathrm{max}} \approx 355$). If we limit our discussions to denser, star-forming regions ($n_{\mathrm{H}} \gtrsim 10^3\,\mathrm{cm^{-3}}$), the agreement is better ($\langle M_F \rangle \sim 300$), meaning that most Ly$\alpha$ photons are absorbed within our computational resolution. It is possible that we over-estimate the feedback effects

around ionization fronts formed in low-density environments because the light travel time for multi-scattered photons can be longer than the simulation time step. However, given that the local photon density and the multiplication factors are usually small ($M_F \lesssim 10$) in these regions, we expect that photoionization heating governs the local gas dynamics, and the uncertainty due to this simplification is likely insignificant.

Another important uncertainty is the lack of internal structures in the star-forming regions. Although our maximum resolution (4.6 pc) is substantially higher than recent large-scale cosmological simulations (e.g. Dubois et al. 2014; Vogelsberger et al. 2014; Schaye et al. 2015; Davé et al. 2017) and at least comparable to zoom-in cosmological simulations (Hopkins et al. 2014; Kimm et al. 2015; Agertz & Kravtsov 2015), GMCs of size $\sim 100\,\mathrm{pc}$ are resolved only by 20 cells across, meaning that the internal structure is unlikely to be captured as realistically as possible. Although the star formation and outflow rates seem reasonably converged (see the Appendix), small-scale simulations find that the dense pillars of gas can self-shield themselves from the radiation, and that star formation continues even after a significant fraction of gas in GMCs is over-pressurised and blown away by radiation (Dale et al. 2012, 2014; Raskutti et al. 2016). The width of such dense filaments from Raskutti et al. (2016) is $\sim 1\,\mathrm{pc}$ or so, which is challenging to achieve in global disk simulations like ours. If these internal structures were present in our simulations, it might be possible to form more stars per cloud, driving more coherent outflows from SNe. However, it is unclear whether there will be enough gas left to be entrained near the GMCs or in the disk, as radiation can disperse them quite effectively.

Finally, the dynamics of gas in our simulations is governed by hydrodynamic interactions and radiation, and any processes associated with magnetic fields are neglected. Hennebelle & Iffrig (2014) shows that magnetic fields not only provide additional pressure support that thickens the gaseous disk, but also suppress the fragmentation of gas clouds by stabilising the Kelvin-Helmholz instability through magnetic tension (Ryu et al. 2000; Hennebelle 2013). The resulting star formation rates are reduced by a factor of two. Given that star formation may become more clustered in the presence of magnetic fields and that magnetic tension can hold the gas more effectively, it will be interesting to see how the reduction in star formation interplays with magnetic fields and drives outflows. We also note that the cosmic ray pressure has a potential to drive strong outflows. As the non-thermal energy cools more slowly ($\gamma = 4/3$) than thermal component of the ideal gas ($\gamma = 5/3$), it is argued that cosmic rays help to build up stable vertical pressure gradient and launch warm ($T \sim 10^4\,\mathrm{K}$) outflows (Uhlig et al. 2012; Booth et al. 2013; Salem & Bryan 2014; Girichidis et al. 2016; Simpson et al. 2016; Pakmor et al. 2016). However, Booth et al. (2013) suggests that the mass loading becomes on the order of unity in a $10^9\,\mathrm{M_\odot}$ dark matter halo when star formation rates become comparable to our simulated galaxies ($\sim 10^{-2}\,\mathrm{M_\odot\,yr^{-1}}$). This is certainly non-negligible, but the relative importance between different physical processes will be unraveled only by running full-blown radiation magneto-hydrodynamic simulations with anisotropic diffusion on galactic scales.

---

[9] We have estimated the computational costs assuming that the MCRT step is done only in every coarse time steps, and found that including the calculations with a small number of photons ($N_{\mathrm{Lya}} = 1000$) can slow down the simulation by more than an order of magnitude, compared to a typical RHD run.

5 CONCLUSIONS

Using a set of radiation-hydrodynamic simulations of a disk galaxy embedded in a small dark matter halo of mass $10^{10}\,\mathrm{M_\odot}$, we investigate the effects of resonantly scattered Lyα photons on the proper-

ties of galaxies and address the issue whether it is possible to drive strong winds by adopting strong radiation feedback. For this purpose, we calculate the multiplication factors of Lyα photons, which boosts the momentum transfer to the gas due to multi-scattering, on a static, uniform medium with a variety of metallicities using a MCRT code, RASCAS (Michel-Dansac et al. *in preparation*), and develop a sub-grid model for the early Lyα feedback in the RAM-SES code (Teyssier 2002; Rosdahl et al. 2013). We also provide fitting functions for the multiplication factors (Eqs. 6–14) which may be useful to the community. Our findings can be summarised as follows.

- In metal-poor systems with low dust content, the multiplication factor can be as high as several hundreds (Fig. 1). In this regime, Lyα pressure is a more efficient feedback process than photo-ionization heating due to LyC photons (Eq. 19) or direct radiation pressure from UV photons, and comparable in momentum to SNe (Fig. 2).

- The momentum input from Lyα pressure operates mostly on cloud scales (Fig. 5), and is able to disrupt star-forming clouds before SNe blow out a significant amount of gas. As a result, the number of SNe exploding in dense environments ($n_{\rm H} \gtrsim 100\,{\rm cm}^{-3}$) is dramatically reduced (Fig. 6), and the star formation rates are suppressed by a factor of two, compared to the RHD run without Lyα feedback (G8R-SN) (Fig. 4).

- The most significant effect of strong early feedback is to smooth out bursty star formation. This leads to weaker galactic outflows, compared to the run without Lyα feedback (Fig. 7). The mass-loading factor measured at $|z| = 2\,{\rm kpc}$ is $\eta_{\rm out} \sim 4$ in the case of G8R-SN-Lya run, whereas it is higher ($\eta_{\rm out} \sim 8$) in the G8R-SN or G8SN runs where star formation is more bursty (Fig. 9). Lyα feedback alone cannot drive strong, extended outflows, as the radiation field drops significantly outside the star-forming clouds.

- We also test the models in which radiation field strength is arbitrarily enhanced by a factor of 3 or 10 and a model in which the star formation efficiency per free-fall time is increased by a factor of 10, but the mass-loading factors are quite similar to those of the fiducial run (G8R-SN-Lya).

- The outflows are not mass-conserving when Lyα feedback is present. The mass-loading factors measured at $0.2\,R_{\rm vir}$ (= $8.2\,{\rm kpc}$) drop to an order of unity in G8R-SN-Lya, whereas it remains nearly unchanged in the G8SN or G8R-SN runs (Fig. 8).

- The inclusion of radiation thickens the disk by providing extra thermal support, and Lyα pressure further increases the scale-height of the disk. The resulting mid-plane pressure and star formation surface densities are good agreement with the models maintaining vertical equilibrium (Fig. 10).

- While long-lived star clusters are allowed to form in the G8R-SN run due to an efficient conversion of gas into stars before the SNe emerge, Lyα pressure not only reduces the number of star clusters but also decreases the typical mass of individual star cluster (Fig. 11).

- Escape fractions of LyC photons are slightly lower in the run with Lyα feedback ($\langle f_{\rm esc}^{\rm LyC} \rangle = 5.5\%$), compared with the SN run ($\langle f_{\rm esc}^{\rm LyC} \rangle = 6.9\%$). This is again because Lyα alone cannot drive strong winds and because SNe become less correlated due to less bursty star formation. In contrast, when the radiation field is strong enough to dominate over SNe, the escape fractions are increased to $\sim 12\%$ (G8R-SN-Lya-f3) or 19% (G8R-SN-Lya-f10). Despite the increase in escape fractions, the total number of escaping LyC photons remains similar within $\sim 20\%$, as the suppression of star formation balances the increase in the escape fraction. This

suggests that the reionization history of the universe is likely not significantly affected by Lyα pressure.

REFERENCES

Abbott D. C., 1982, ApJ, 259, 282
Adams T. F., 1972, ApJ, 174, 439
Adams T. F., 1975, ApJ, 201, 350
Agertz O., Kravtsov A. V., 2015, ApJ, 804, 18
Agertz O., Kravtsov A. V., 2016, ApJ, 824, 79
Agertz O., Kravtsov A. V., Leitner S. N., Gnedin N. Y., 2013, ApJ, 770, 25
Aumer M., White S. D. M., Naab T., Scannapieco C., 2013, MNRAS, 434, 3142
Behroozi P. S., Wechsler R. H., Conroy C., 2013, ApJ, 770, 57
Bieri R., Dubois Y., Rosdahl J., Wagner A., Silk J., Mamon G. A., 2017, MNRAS, 464, 1854
Bisbas T. G., et al., 2015, MNRAS, 453, 1324
Bithell M., 1990, MNRAS, 244, 738
Blondin J. M., Wright E. B., Borkowski K. J., Reynolds S. P., 1998, ApJ, 500, 342
Bonilha J. R. M., Ferch R., Salpeter E. E., Slater G., Noerdlinger P. D., 1979, ApJ, 233, 649
Booth C. M., Agertz O., Kravtsov A. V., Gnedin N. Y., 2013, ApJ, 777, L16
Breitschwerdt D., McKenzie J. F., Voelk H. J., 1991, A&A, 245, 79
Callaway J., Unnikrishnan K., Oza D. H., 1987, Phys. Rev. A, 36, 2576
Campello R. J. G. B., Moulavi D., Sander J., 2013, Density-Based Clustering Based on Hierarchical Density Estimates. Springer Berlin Heidelberg, Berlin, Heidelberg, pp 160–172, doi:10.1007/978-3-642-37456-2_14, https://doi.org/10.1007/978-3-642-37456-2_14
Cantalupo S., Porciani C., Lilly S. J., 2008, ApJ, 672, 48
Cardelli J. A., Clayton G. C., Mathis J. S., 1989, ApJ, 345, 245
Castor J. I., Abbott D. C., Klein R. I., 1975, ApJ, 195, 157
Chisholm J., Tremonti C. A., Leitherer C., Chen Y., 2017, MNRAS, 469, 4831
Dale J. E., Ercolano B., Bonnell I. A., 2012, MNRAS, 424, 377
Dale J. E., Ngoumou J., Ercolano B., Bonnell I. A., 2014, MNRAS, 442, 694
Davé R., Rafieferantsoa M. H., Thompson R. J., Hopkins P. F., 2017, MNRAS, 467, 115
Davis S. W., Jiang Y.-F., Stone J. M., Murray N., 2014, ApJ, 796, 107
Devriendt J., et al., 2010, MNRAS, 403, L84

Devriendt J. E. G., Slyz A., Kimm T., Richardson M., 2017, in prep
Dijkstra M., 2014, Publ. Astron. Soc. Australia, 31, e040
Dijkstra M., Loeb A., 2008, MNRAS, 391, 457
Dijkstra M., Haiman Z., Spaans M., 2006, ApJ, 649, 14
Draine B. T., 2011a, Physics of the Interstellar and Intergalactic Medium
Draine B. T., 2011b, ApJ, 732, 100
Draine B. T., et al., 2007, ApJ, 663, 866
Dubois Y., et al., 2014, MNRAS, 444, 1453
Engelbracht C. W., Rieke G. H., Gordon K. D., Smith J.-D. T., Werner M. W., Moustakas J., Willmer C. N. A., Vanzi L., 2008, ApJ, 678, 804
Evans II N. J., Heiderman A., Vutisalchavakul N., 2014, ApJ, 782, 114
Everett J. E., Zweibel E. G., Benjamin R. A., McCammon D., Rocks L., Gallagher III J. S., 2008, ApJ, 674, 258
Federrath C., Klessen R. S., 2012, ApJ, 761, 156
Finlator K., Davé R., 2008, MNRAS, 385, 2181
Fisher D. B., et al., 2013, preprint, (arXiv:1310.4842)
Forbes J. C., Krumholz M. R., Goldbaum N. J., Dekel A., 2016, Nature, 535, 523
Galametz M., Madden S. C., Galliano F., Hony S., Bendo G. J., Sauvage M., 2011, A&A, 532, A56
Gavagnin E., Bleuler A., Rosdahl J., Teyssier R., 2017, preprint, (arXiv:1701.07982)
Geen S., Hennebelle P., Tremblin P., Rosdahl J., 2016, MNRAS, 463, 3129
Gentry E. S., Krumholz M. R., Dekel A., Madau P., 2017, MNRAS, 465, 2471
Georgiev I. Y., Puzia T. H., Goudfrooij P., Hilker M., 2010, MNRAS, 406, 1967
Girichidis P., et al., 2016, ApJ, 816, L19
Gnedin N. Y., Abel T., 2001, New Astronomy, 6, 437
Gnedin N. Y., Tassis K., Kravtsov A. V., 2009, ApJ, 697, 55
Górski K. M., Hivon E., Banday A. J., Wandelt B. D., Hansen F. K., Reinecke M., Bartelmann M., 2005, ApJ, 622, 759
Guiderdoni B., Rocca-Volmerange B., 1987, A&A, 186, 1
Guillet T., Teyssier R., 2011, Journal of Computational Physics, 230, 4756
Haardt F., Madau P., 2012, ApJ, 746, 125
Hanasz M., Lesch H., Naab T., Gawryszczak A., Kowalik K., Wóltański D., 2013, ApJ, 777, L38
Hansen M., Oh S. P., 2006, MNRAS, 367, 979
Harrington J. P., 1973, MNRAS, 162, 43
Heckman T. M., Alexandroff R. M., Borthakur S., Overzier R., Leitherer C., 2015, ApJ, 809, 147
Hennebelle P., 2013, A&A, 556, A153
Hennebelle P., Iffrig O., 2014, A&A, 570, A81
Hill A. S., Joung M. R., Mac Low M.-M., Benjamin R. A., Haffner L. M., Klingenberg C., Waagan K., 2012, ApJ, 750, 104
Hillas A. M., 2005, Journal of Physics G Nuclear Physics, 31, R95
Hopkins P. F., Quataert E., Murray N., 2011, MNRAS, 417, 950
Hopkins P. F., Quataert E., Murray N., 2012, MNRAS, 421, 3522
Hopkins P. F., Kereš D., Oñorbe J., Faucher-Giguère C.-A., Quataert E., Murray N., Bullock J. S., 2014, MNRAS, 445, 581
Hu C.-Y., Naab T., Glover S. C. O., Walch S., Clark P. C., 2017, MNRAS, 471, 2151
Hui L., Gnedin N. Y., 1997, MNRAS, 292, 27
Iffrig O., Hennebelle P., 2015, A&A, 576, A95
Joung M. R., Cen R., Bryan G. L., 2009a, ApJ, 692, L1
Joung M. R., Mac Low M.-M., Bryan G. L., 2009b, ApJ, 704, 137
Katz N., 1992, ApJ, 391, 502
Katz H., Kimm T., Sijacki D., Haehnelt M. G., 2017, MNRAS, 468, 4831
Keller B. W., Wadsley J., Benincasa S. M., Couchman H. M. P., 2014, MNRAS, 442, 3013
Kennicutt Jr. R. C., 1998, ApJ, 498, 541
Kim C.-G., Ostriker E. C., 2015, ApJ, 802, 99
Kim C.-G., Ostriker E. C., Kim W.-T., 2013, ApJ, 776, 1
Kim J.-G., Kim W.-T., Ostriker E. C., 2016, ApJ, 819, 137
Kim C.-G., Ostriker E. C., Raileanu R., 2017, ApJ, 834, 25
Kimm T., Cen R., 2014, ApJ, 788, 121
Kimm T., Cen R., Devriendt J., Dubois Y., Slyz A., 2015, MNRAS, 451, 2900

Kimm T., Cen R., Rosdahl J., Yi S. K., 2016, ApJ, 823, 52
Kimm T., Katz H., Haehnelt M., Rosdahl J., Devriendt J., Slyz A., 2017, MNRAS, 466, 4826
Kravtsov A. V., Gnedin O. Y., 2005, ApJ, 623, 650
Kroupa P., 2001, MNRAS, 322, 231
Krumholz M. R., Thompson T. A., 2012, ApJ, 760, 155
Krumholz M. R., Stone J. M., Gardiner T. A., 2007, ApJ, 671, 518
Leitherer C., et al., 1999, ApJS, 123, 3
Leroy A. K., et al., 2015, ApJ, 814, 83
Lisenfeld U., Ferrara A., 1998, ApJ, 496, 145
Lopez L. A., Krumholz M. R., Bolatto A. D., Prochaska J. X., Ramirez-Ruiz E., Castro D., 2014, ApJ, 795, 121
Maiolino R., et al., 2008, A&A, 488, 463
Martizzi D., Faucher-Giguère C.-A., Quataert E., 2015, MNRAS, 450, 504
Matzner C. D., 2002, ApJ, 566, 302
Moster B. P., Naab T., White S. D. M., 2013, MNRAS, 428, 3121
Muratov A. L., Kereš D., Faucher-Giguère C.-A., Hopkins P. F., Quataert E., Murray N., 2015, MNRAS, 454, 2691
Murray N., Quataert E., Thompson T. A., 2005, ApJ, 618, 569
Neufeld D. A., 1990, ApJ, 350, 216
Oppenheimer B. D., Davé R., 2008, MNRAS, 387, 577
Osterbrock D. E., 1962, ApJ, 135, 195
Osterbrock D. E., Ferland G. J., 2006, Astrophysics of gaseous nebulae and active galactic nuclei
Ostriker E. C., McKee C. F., Leroy A. K., 2010, ApJ, 721, 975
Paardekooper J.-P., Khochfar S., Dalla Vecchia C., 2015, MNRAS, 451, 2544
Padoan P., Nordlund Å., 2011, ApJ, 730, 40
Padoan P., Pan L., Haugbølle T., Nordlund Å., 2016, ApJ, 822, 11
Pakmor R., Pfrommer C., Simpson C. M., Springel V., 2016, ApJ, 824, L30
Partridge R. B., Peebles P. J. E., 1967, ApJ, 147, 868
Pontzen A., Governato F., 2012, MNRAS, 421, 3464
Rasera Y., Teyssier R., 2006, A&A, 445, 1
Raskutti S., Ostriker E. C., Skinner M. A., 2016, ApJ, 829, 130
Read J. I., Iorio G., Agertz O., Fraternali F., 2017, MNRAS, 467, 2019
Rémy-Ruyer A., et al., 2014, A&A, 563, A31
Rosdahl J., Blaizot J., 2012, MNRAS, 423, 344
Rosdahl J., Teyssier R., 2015, MNRAS, 449, 4380
Rosdahl J., Blaizot J., Aubert D., Stranex T., Teyssier R., 2013, MNRAS, 436, 2188
Rosdahl J., Schaye J., Teyssier R., Agertz O., 2015, MNRAS, 451, 34
Ryu D., Jones T. W., Frank A., 2000, ApJ, 545, 475
Salem M., Bryan G. L., 2014, MNRAS, 437, 3312
Sawala T., et al., 2015, MNRAS, 448, 2941
Schaye J., et al., 2015, MNRAS, 446, 521
Schmidt M., 1959, ApJ, 129, 243
Sharma P., Roy A., Nath B. B., Shchekinov Y., 2014, MNRAS, 443, 3463
Simpson C. M., Pakmor R., Marinacci F., Pfrommer C., Springel V., Glover S. C. O., Clark P. C., Smith R. J., 2016, ApJ, 827, L29
Skinner M. A., Ostriker E. C., 2015, ApJ, 809, 187
Smith A., Bromm V., Loeb A., 2016, MNRAS, 460, 3143
Smith A., Tsang B. T.-H., Bromm V., Milosavljevic M., 2017a, preprint, (arXiv:1709.10187)
Smith A., Bromm V., Loeb A., 2017b, MNRAS, 464, 2963
Springel V., Di Matteo T., Hernquist L., 2005, MNRAS, 361, 776
Stanway E. R., Eldridge J. J., Becker G. D., 2016, MNRAS, 456, 485
Teyssier R., 2002, A&A, 385, 337
Teyssier R., Pontzen A., Dubois Y., Read J. I., 2013, MNRAS, 429, 3068
Thornton K., Gaudlitz M., Janka H.-T., Steinmetz M., 1998, ApJ, 500, 95
Toro E. F., Spruce M., Speares W., 1994, Shock Waves, 4, 25
Trebitsch M., Blaizot J., Rosdahl J., Devriendt J., Slyz A., 2017, preprint, (arXiv:1705.00941)
Truelove J. K., Klein R. I., McKee C. F., Holliman II J. H., Howell L. H., Greenough J. A., 1997, ApJ, 489, L179
Uhlig M., Pfrommer C., Sharma M., Nath B. B., Enßlin T. A., Springel V., 2012, MNRAS, 423, 2374
Verhamme A., Schaerer D., Maselli A., 2006, A&A, 460, 397
Vogelsberger M., et al., 2014, MNRAS, 444, 1518

Walch S. K., Whitworth A. P., Bisbas T., Wünsch R., Hubber D., 2012, MNRAS, 427, 625

Walch S., et al., 2015, MNRAS, 454, 238

Weingartner J. C., Draine B. T., 2001, ApJ, 548, 296

Wise J. H., Cen R., 2009, ApJ, 693, 984

Wise J. H., Demchenko V. G., Halicek M. T., Norman M. L., Turk M. J., Abel T., Smith B. D., 2014, MNRAS, 442, 2560

deAvillez M. A., Breitschwerdt D., 2005, A&A, 436, 585

APPENDIX

We note that our resolution (2.3–4.6 pc) may not be high enough to resolve the detailed turbulent structure inside a GMC, and the propagation of ionization fronts may be affected by the finite resolution. However, the eventual (D-type) expansion of a HII region in dense environments is driven by the over-pressure inside the bubble, and the radial extent to which photoionization heating or Lyα pressure can counterbalance the ambient pressure is generally larger than our resolution (Eq. 19–20). Therefore, we expect that the star formation histories of our simulated galaxies should not be affected by resolution. To demonstrate this, we perform resolution tests in Figure 16. Specifically, we run two additional simulations with one more and one fewer levels of refinement (minimum cell widths of 2.3 pc and 9.2 pc, respectively), keeping other parameters fixed, except for the minimum gas mass to trigger the refinement in the high resolution run (125 $M_\odot$ instead of 1000 $M_\odot$ for the higher resolution run). It can be seen that both the star formation histories and outflow rates are reasonably converged. In the early collapsing phase ($t \lesssim 50$ Myr), the higher resolution runs show systematically higher star formation rates, because the gaseous disk fragments more efficiently. Accordingly, outflow rates are slightly more enhanced in the higher resolution runs during the first ~ 200 Myr. However, as soon as the collapsing phase ends, the star formation rates averaged over 50 Myr settle around $\sim 0.01 \, M_\odot \, yr^{-1}$, and the mass-loading factors become similar between these runs, indicating that the simulation results are converged at several pc resolutions. We also check that the properties of the ISM are reasonably similar, although the high resolution run yields slightly thicker disk (73 pc vs 80 pc) due to stronger mid plane pressure ($P/K = 10^{4.7} \, cm^{-3} \, K$ vs $P/K = 10^{4.9} \, cm^{-3} \, K$).
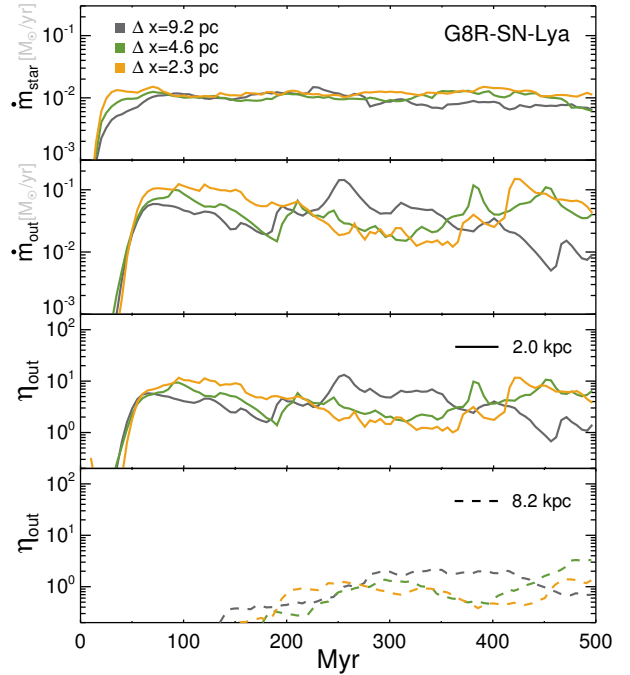

Figure 16. Resolution test of the runs with Lyα pressure. From top to bottom, each panel shows the star formation rates in $M_\odot \, yr^{-1}$, the outflow rates measured at $|z| = 2$ kpc, the mass-loading factors measured at $|z| = 2$ kpc and $|z| = 0.2 \, R_{vir}$ (8.2 kpc).